Review on Modeling and Simulation of Continuous Casting

*Brian G. Thomas**

Continuous casting is a mature, sophisticated technological process, used to produce most of the world's steel, so is worthy of fundamentally-based computational modeling. It involves many interacting phenomena including heat transfer, solidification, multiphase turbulent flow, clogging, electromagnetic effects, complex interfacial behavior, particle entrapment, thermal-mechanical distortion, stress, cracks, segregation, and microstructure formation. Furthermore, these phenomena are transient, three-dimensional, and operate over wide length and time scales. This paper reviews the current state of the art in modeling these phenomena, focusing on practical applications to the formation of defects. It emphasizes model verification and validation of model predictions. The models reviewed range from fast and simple for implementation into online model-based control systems to sophisticated multiphysics simulations that incorporate many coupled phenomena. Both the accomplishments and remaining challenges are discussed.

1. Introduction

The continuous casting process is used in making over 96% of steel products in the world, as of 2015.[1] It is a mature and sophisticated technological process that has undergone decades of improvements, based mainly on experience with the commercial operation, aided by physical water modeling to understand the fluid flow behavior. Further advances will require better understanding of the fundamental behaviors, which is difficult with experiments, owing to the harsh environment. This makes continuous casting an ideal process for advanced computational simulation, which has improved significantly in recent years.[2]

The challenge for modeling is to accurately predict something of practical use to designers and practitioners, such as the formation of defects. Unfortunately, this is very difficult, because like most real commercial processes, the continuous casting of steel is governed by an extremely complex system of inter-related phenomena, a few of which are illustrated in **Figure 1**.[3] Furthermore, most of these phenomena require a fully three-dimensional domain and involve wide ranges of both length and time scales. For example, initial solidification at the meniscus, which govern surface defects, involves a size scale much less than one millimeter, while nucleation occurring there is well known to affect centerline segregation, that occurs more than 10 m away. The time scale of turbulent eddies that govern the capture of particles between dendrites is in milliseconds, while instabilities in mold surface level caused by bulging instabilities between rolls in the secondary cooling zones are known to evolve over several hours. An accurate computational model of phenomena, such as these must find ways to bridge these great gaps in length and time scale, and is a daunting task.

The staggering complexity of the continuous-casting process makes it impossible to model all of these phenomena together at once. Thus, it is necessary to make reasonable assumptions and to uncouple or neglect the less-important phenomena, according to a specific purpose chosen for the model. Choosing the model purpose is thus the most critical modeling step. One major purpose of useful models is to gain new insights into understanding some aspect of the process, such as explaining the mechanism(s) of how a particular defect likely formed, and how its incidence is affected by controllable process variables.

Having chosen the domain and governing equations, they can be discretized and solved using numerical methods, such as finite-difference for fluid flow and finite-element for stress analysis. It is important that adequate numerical validation be conducted. Numerical errors commonly arise from too coarse a computational domain or incomplete convergence when solving the nonlinear equations. Solving a known test problem and conducting mesh refinement studies to a achieve grid independent solution is an important first step to verify the model. Finally, a model must be calibrated and validated against experimental measurements on both the laboratory and plant scales before it can be trusted to gain quantitative understanding of the real process from parametric studies.

This paper reviews some of the recent advances in modeling steel continuous casting, which have been accomplished by many research groups around the world. Space permits just a few examples, which are taken mainly from slab casting with mold slag, and from the results of my own research group, owing to familiarity with this work. Space also permits referencing only a fraction of the high-quality research that has been done on this

Prof. B. G. Thomas
Professor of Mechanical Engineering
Colorado School of Mines, Brown Hall W370-B,
1610 Illinois Street, Golden, CO 80401
E-mail: bgthomas@mines.edu

The ORCID identification number(s) for the author(s) of this article can be found under https://doi.org/10.1002/srin.201700312.

DOI: 10.1002/srin.201700312

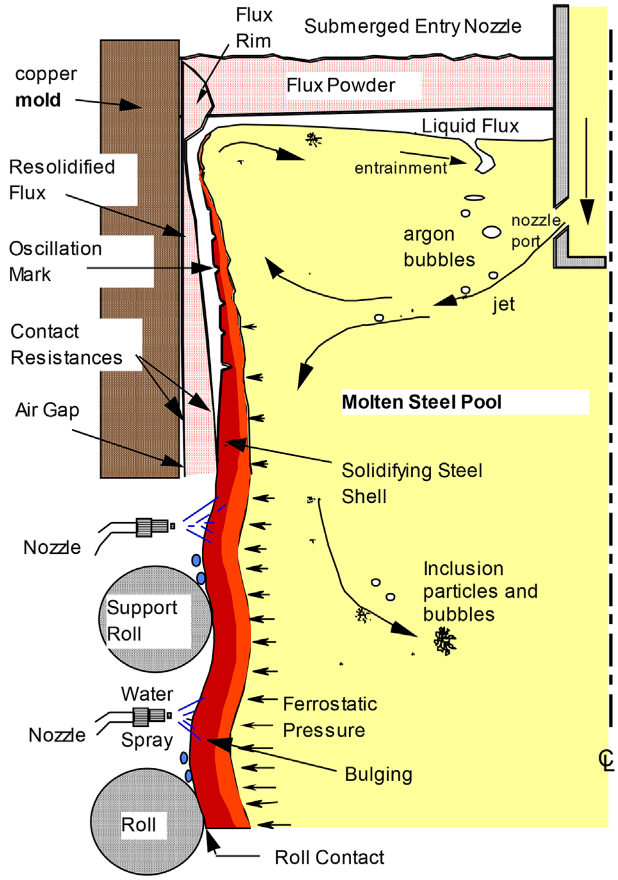

Figure 1. Fluid-flow phenomena in the mold region of a steel slab caster. Reproduced with permission.[3] 2002, TMS.

Dr. Brian G. Thomas is Professor of Mechanical Engineering at the Colorado School of Mines, Golden, CO, USA, and Director of the Continuous Casting Center. He is also Gauthier Professor Emeritus at the University of Illinois, Urbana, Illinois. His research efforts focus on computational modeling of continuous casting of steel and related processes.

very large and popular subject. An emphasis is made on model validation, because many recent models combine together several complex phenomena for the first time, and comparison with actual plant measurements is the only way to check if these complex models are reasonable. Every aspect of every model should be both verified with known solutions and validated with measurements in order to trust the predictions of computational models and suggested improvements arising from modeling studies. Such efforts are worthwhile, because plant experiments aiming to improve this mature process take a long time to evaluate, and at significant cost, especially if they are wrong.

2. Heat Transfer and Solidification

Continuous casting is fundamentally a heat-transfer process, removing the superheat, latent heat, and some sensible heat from the molten metal to produce a solid strand with a desired cross-sectional shape and size. Models to predict temperature distribution and growth of the solidifying steel shell are needed for basic design, trouble shooting, and control of the process. They are also a crucial building block for many advanced computational models, which couple heat transport together with other phenomena. These models solve the transient heat conduction equation, where latent heat may be introduced via several different numerical techniques, which are reviewed elsewhere.[4,5]

The most difficult task in development of an accurate solidification heat-transfer model of continuous casting is to accurately model heat removal from the strand surface. This is especially an issue in the mold, where heat transfer is governed mainly by heat conduction across the interfacial gap between the shell and the mold wall. Heat transfer below the mold also presents challenges, owing to the complex phenomena such as droplet impingement and film boiling that occur at the strand surface during spray and air-mist cooling, and from roll contact. The simplest approach is to calibrate the model to match plant measurements, which is both popular and effective.[6–12] To extend the model to other casting conditions, however, a more fundamental approach is desired as well.

Calibration of solidification heat-transfer models in the mold can exploit measurements such as cooling-water heatup for a global energy balance, thermocouple temperatures in the mold walls for the heat-flux profile, and shell thickness measurements from breakout shells or composition profiles after trace-metal injection.[6–8,13–16] This can be accomplished using trial and error[9,13,17,18] or an inverse model,[8,9,19] with either a full 3D model[7,9,15–17,19–21] or an accurate reduced-order model of the mold wall geometry.[13,14,22,23] An example is shown in **Figure 2**, where interfacial parameters in the model were calibrated to match mold temperatures, and then comparison with the breakout shell profile represents model validation.[13] Note that the prediction for steady-state conditions differs somewhat from the profile predicted under the transient conditions, when the breakout occurred, which naturally matches better with the measurements.[13]

Model validation with plant measurements below the mold is more difficult. Surface temperature can be measured in the spray zones, but pyrometer readings are lowered by steam and surface oxide scale formation. Shell thickness typically involves indirect observations, such as tracer injection,[6] strand thermocouples,[22] relative roll force,[24] roll movement,[24] internal hot-tears induced by inserting shims between the strand and the rolls,[14] the melted tips of nails shot into the strand,[25] or the serious defect of whale formation, which occurs when the metallurgical length exceeds the supported length of the strand.[10,24] For example, the shell thickness predictions in **Figure 3** were validated indirectly by the model agreement with both roll movement measurements,[24] and with many plant instances with and without whale formation.[10] The surface temperature predictions only agree with the pyrometer

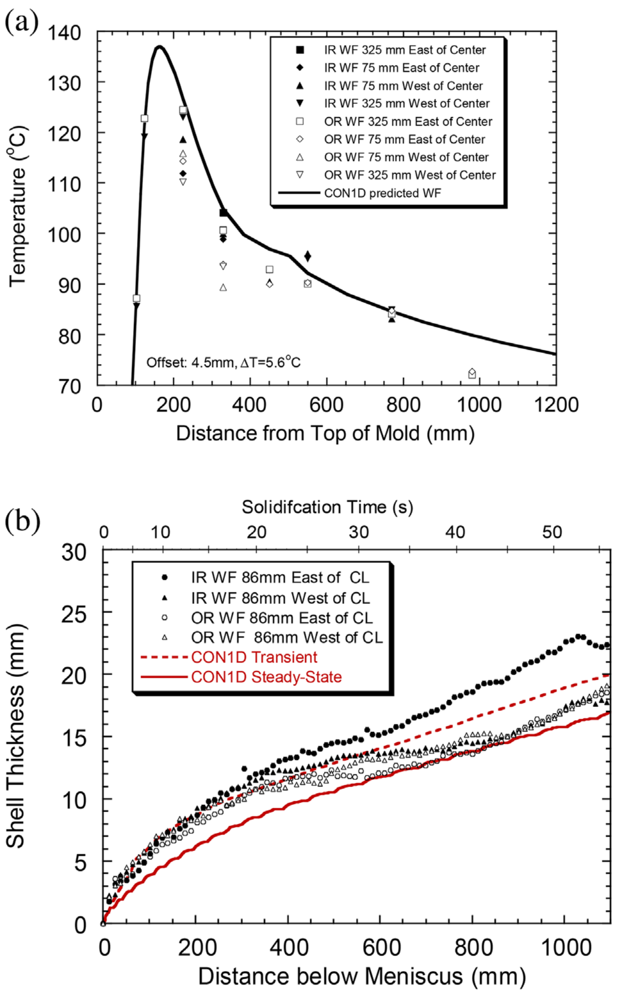

Figure 2. a) Temperature in the mold wall, comparing predictions with thermocouple measurements.[13] b) Solidified shell thickness in the mold, comparing predictions (lines), and breakout shell measurements (symbols). Reproduced with permission.[13] 2006, The Iron and Steel Institute of Japan.

measurements lower in the caster and during reheating after caster exit.[10] When accurate pyrometer measurements are available, an inverse model can be applied to match the predicted surface temperature profile with the peaks of those measurements, to overcome dips caused by intermittent scale.[12] Finally, the shell thickness predictions near final solidification of several models have been successfully validated with nail shooting measurements.[12,25–28]

Once validated, simple heat transfer solidification models have a wide range of powerful practical applications, which have had great impact on improving the process in commercial practice. For example, post-mortem analysis of the location and cause of internal hot-tear cracks can be inferred from model predictions of the location of the critical temperature range near the solidification front. Another important example is determination of the solid fraction profile near final solidification. In addition to finding the maximum casting speed to avoid whale formation,[24] such models can be used to help choose the best position of soft reduction equipment[27,29] or final electro-magnetic stirring equipment.[12,25,26,28] for the mitigation of centerline defects.

2.1. Interfacial Heat Transfer

Many detailed models have been developed to predict heat transfer across the interfacial gap between the strand and the mold wall in a fundamental manner.[13,15–17,19,22,30–37] Interfacial heat transfer depends on the thermal conductivity of the interfacial layers and the size of the gap, which requires both detailed models of the gap and measurements. Lab measurements of mold slag thermal conductivity must be interpreted using models to extract the property data from the raw measurements. Both thermal conductivity and slag viscosity depend greatly on the extent of crystallization, which is a complex process that can be characterized as C-shaped curves in time–temperature–transformation diagrams.[13,32] This means that the slag properties properly require more

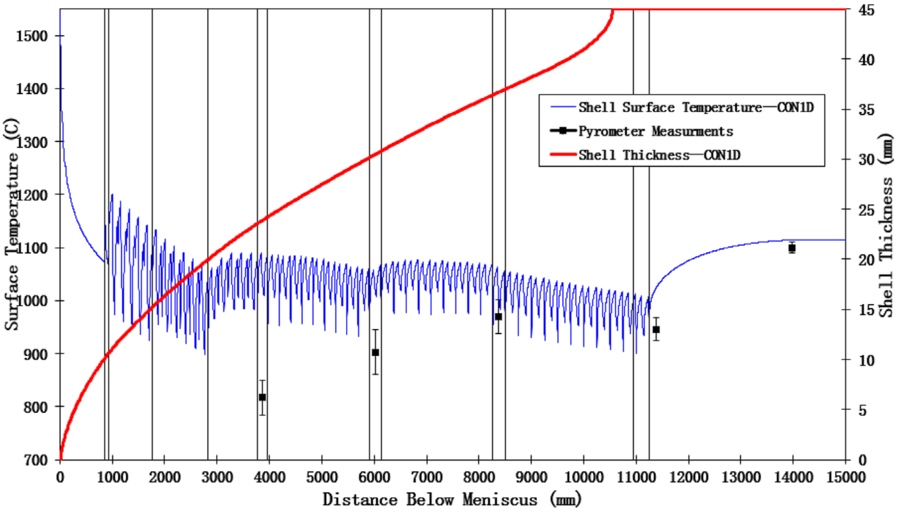

Figure 3. Strand surface-temperature predictions compared with pyrometer measurements and shell thickness profile. Reproduced with permission.[10] 2011, TMS.

than simple temperature-dependent functions, which complicates gap models.

Contact resistance between the solidified, typically de-vitrified, slag layer, and the mold wall depends on the roughness of the solid slag surface, and is greatly affected by slag composition. One approach to model this challenging problem is to consider that the slag against the mold wall should continue to flow and flatten until it either crystallizes or its viscosity becomes extremely high, as characterized by its cooling below the glass transition temperature.[13] Surface roughness is then defined by the distance from the mold wall to the isotherm in the slag layer corresponding to that transition temperature.[13]

Over most of the strand surface, the gap thickness depends on the balance between liquid slag infiltration at the meniscus due to mold oscillation and the consumption of the slag as it is dragged downward by the strand at the casting speed, while being squeezed by the ferrostatic pressure from the internal liquid pool transmitted through the shell. Thus, a model of thermal-flow and mass conservation of the slag is useful for tracking the thickness of the liquid and solid slag layers along the gap,[13,15,22,32,37] and can be validated with measured slag films.[13,37] The oscillation marks greatly affect the gap and consume a significant amount of slag, so deeper oscillation marks or surface depressions have higher slag consumption, and should be taken into account as well.[22,38,39]

Toward the corners of the strand in the mold, the ferrostatic pressure is unable to overcome shrinkage of the strand to maintain good contact between the shell and the mold. Thus, when the corner regions are important, a two-way coupled thermo-mechanical model can be combined with the interfacial gap model to determine the size of the gap as it varies in space and time. Such models should also consider taper of the mold walls and thermal distortion of both the mold and shell, as discussed later.

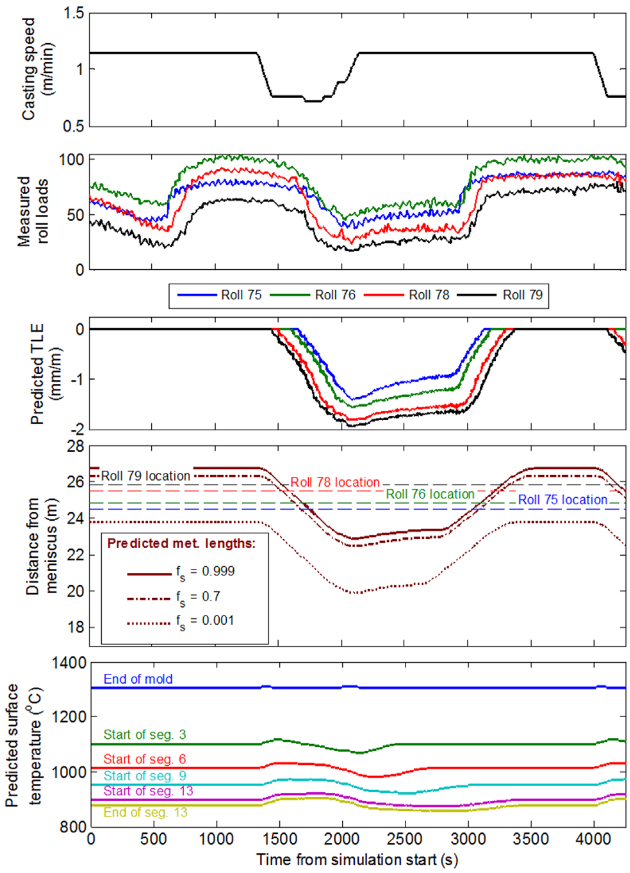

Figure 4. Model predictions of dynamic surface temperature, metallurgical length, and thermal shrinkage, compared with measured roll loads, during a dip in casting speed. Reproduced with permission.[24] 2015, AIST.

2.2. Online Control

Fundamentally-based computational models of heat transfer and solidification are now sufficiently accurate and efficient, that they are being used as part of online control systems.[10,24,26,40–42] For typical commercial casting speeds, the advection of heat by the moving strand is much larger than heat conduction in the casting direction.[22] This enables Lagrangian thermal-solidification models of a horizontal slice moving down through the strand, which are efficient enough to run in real time.[10,24]

While validation of steady-state thermal models has become standard practice in development of most models of continuous casting of steel, validation under transient conditions is rare. **Figure 4** shows an example comparing indirect plant measurements of metallurgical length under transient conditions with predictions of a dynamic thermal solidification model in a conventional thick slab caster.[24] The top frame shows the casting speed history, where attention is focused on a dip in casting speed. The second frame shows strain gauge measurements taken in four rolls located near the metallurgical length during this time. The speed drop changes the total thermal linear expansion (TLE), or average shrinkage strain through the strand thickness, the metallurgical length, and the surface temperature histories predicted by the model, which are shown in the remaining three frames of this figure. While the strand has a liquid core, the internal liquid ferrostatic pressure generates high loads in the support rolls. During the casting speed dip, frame 3 shows that the metallurgical length decreases, so that the strand beneath all four rolls is completely solid, and generates low measured loads.

The predicted TLE, which is reported relative to zero, when liquid is present in the core, has the same qualitative behavior. More remarkable is the agreement between the predicted dynamic transition times and the measurements. Both the measured loads and the predicted TLE signals experience a gradual decline, with a short delay after the initial drop in speed, which begin in sequence from rolls. Then, both signals slowly increase while the speed stays low. Finally, a relatively fast rise in both signals follows in the opposite order of rolls from 75 to 79, and with a much longer delay after the final speed rise. As the model was calibrated only for steady-state conditions, this quantitative match with the measured transition times under transient conditions indicates model validation.[24]

Advanced thermal-solidification models are also used online for other control purposes, such as determining the solid fraction profile near final solidification, for positioning of dynamic soft reduction.[29] The use of fundamentally-based models in control systems will continue to grow.

3. Fluid Flow Modeling

Many investigations of fluid flow in the steel continuous casting nozzle and mold have been conducted using three-dimensional computational fluid dynamics (CFD) models, and has been the subject of previous reviews.[43,44] These models solve the continuity equation for conserving mass, and the Navier–Stokes equations for conserving the momentum of incompressible Newtonian fluids, such as steel, using classical finite-volume, or finite-difference methods, often with commercial CFD software, such as the ANSYS-FLUENT code.[45] Results in the form of quantitative versions of Figure 1 are numerous, and include many realistic animations of the turbulent flow.

The most popular numerical approach is to assume steady-state, single-phase flow, using a Reynold's Averaged Navier–Stokes (RANS) method, together with a turbulence model such as k-ε, or k-ω SST, which is designed to estimate the average effect of turbulence,[43] based on solving extra transport equations which depend on calibrated empirical parameters.[46] RANS models are very computationally-efficient and are reasonably accurate for estimating the steady-state flow pattern, owing to their use of empirical wall-law boundary conditions which can capture the sharp velocity gradients in the boundary layers with a coarse grid.[44] Although transient behavior is less accurate with RANS models,[47] unsteady RANS models have been applied recently to estimate transient flow, with some success.[48–50] Large Eddy Simulation (LES) can more accurately resolve the details of transient flow, owing to its use of finer grids and smaller time steps to resolve the turbulent flow, and sub-grid-scale turbulence models which lessen the importance of the empirical turbulence-model parameters as the grid becomes increasingly refined. However, this required grid refinement makes LES much more computationally expensive. As computer hardware, and software tools such as parallel solvers using graphics processing units,[51] have become more powerful, the application of LES models to continuous casting has become more popular in recent years.[52–61]

3.1. Fluid Flow in the Nozzle

The flow velocity and pressure distributions in the metal delivery system to the caster, including the tundish, flow control system (stopper rod or slide gate), and the submerged entry nozzle are very important to steel quality. This is because they control: 1) air aspiration which is a source reoxidation and inclusions, if the pressure becomes negative near a joint in the refractories, 2) nozzle clogging due to inclusion particle agglomeration on the nozzle walls, and 3) the flow rate in the entire process, including the flow pattern and level fluctuations in the mold.

Computational models of the nozzle have included the slide-gate,[62–64] the stopper rod,[65,66] or the refractory-funnel-nozzle semi-open-pouring flow control system,[67] which greatly affects the flow in both the nozzle and the mold cavity.[68] Many models have simulated the important effects of argon gas injection on turbulent flow inside the nozzle,[62–64] and also in the mold.[58,60,61,66,69–88] These models depend on the bubble size distribution, which is very difficult to determine, even experimentally, as water models are unreliable owing to their property differences compared with molten metals. Models show that argon bubbles in steel are larger than air bubbles in water for similar conditions, for example.[85,89] Computational approaches to handle this problem are discussed later.

3.2. Nozzle Clogging

The attachment and buildup of inclusion particles to the refractory walls of the nozzle leads to nozzle clogging. In addition to lowering productivity, clogging is detrimental to steel quality due to the releasing of clogs, which generates both large inclusions and unstable flow in the mold, leading to excessive surface level fluctuations.[90] Nozzle clogging has been investigated using models to simulate the inclusion attachment process by a few researchers.[64,90–92] In these models, particle transport and attachment can be modeled using a fluid flow model for the velocity and pressure fields, combined with a Lagrangian particle tracking method, such as the Discrete Particle Method (DPM)[93–96] for the inclusions. Argon gas can disrupt this clogging process, by changing the flow pattern.[90] Clogging also depends greatly on the compositions of the inclusion and nozzle refractory surfaces, and whether the inclusions are liquid or solid, which requires thermodynamic modeling.[97]

Clogging can also be caused by inclusions generated from reoxidation, via exposure of the steel stream during open-stream pouring or by aspiration of air through cracks and joints in the nozzle in submerged casting. Reoxidation has been modeled in free stream pouring by adding an oxygen transport model and an oxide formation model to a fluid flow model.[98] The reoxidation rate depends on the exposed surface area, and the saturation extent of the molten steel.

Modeling the pressure distribution inside the nozzle can provide important insights into nozzle clogging, as aspiration-based clogging is most likely when the pressure drops below atmospheric pressure. Several previous models have applied CFD models to predict these pressure distributions.[62,63] These models found that aspiration can be mitigated by decreasing the tundish depth, decreasing the upper tundish nozzle, and submerged entry nozzle inner-bore diameters, and/or by increasing the argon gas flow rate, thereby causing the flow control to open more which lessens the local pressure drop.

3.3. Reduced-Order Flow Models

It is often useful to obtain a quick estimate of certain phenomena, which are significant but peripheral to a project, without developing a full, three-dimensional computational model of that aspect of the process. This can be accomplished using analytical solutions or with "reduced order" models. For example, the pressure distribution and corresponding flow rate through the liquid metal delivery system, is needed for online control models, parametric studies, and as input to mold flow models. This pressure distribution can be estimated using a simple energy-balance approach based on a Bernoulli-type analysis of turbulent pipe flow.[99] Such simple models can match reasonably well with both a multiphase Eulerian/Eulerian numerical model of the flow, (**Figure 5**) and with plant measurements (**Figure 6**), considering that the top surface pressures in both tundish and mold are predicted to be near 1 atm for the given plant conditions.[100]

Both models predict negative pressure below the slide gate. Considering that the grooves in the slide gate plates are supplied with argon gas to avoid air aspiration, these joints will allow passive flow of argon gas into the low-pressure region below the slide gate. If leaks are excessive or if argon flow is insufficient, severe reoxidation can occur. The argon flow rate needed to sustain positive pressure inside the nozzle (above 1 atm) can be predicted with these models.[100]

3.4. Argon Gas Injection

Argon gas is commonly injected into the Upper Tundish Nozzle to help prevent clogging. After being delivered through a gas line above the slide-gate, it typically diffuses through porous portions of the nozzle refractory to exit the inner-bore surface into the flowing steel, as shown in **Figure 7**a.

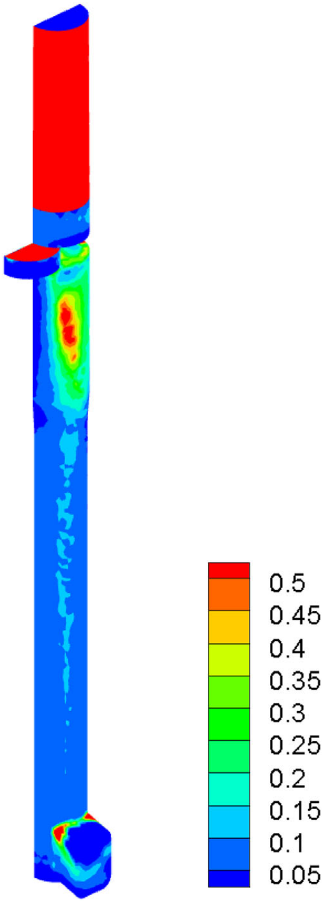

Figure 5. Gas volume fraction in a slide-gate nozzle.[100]

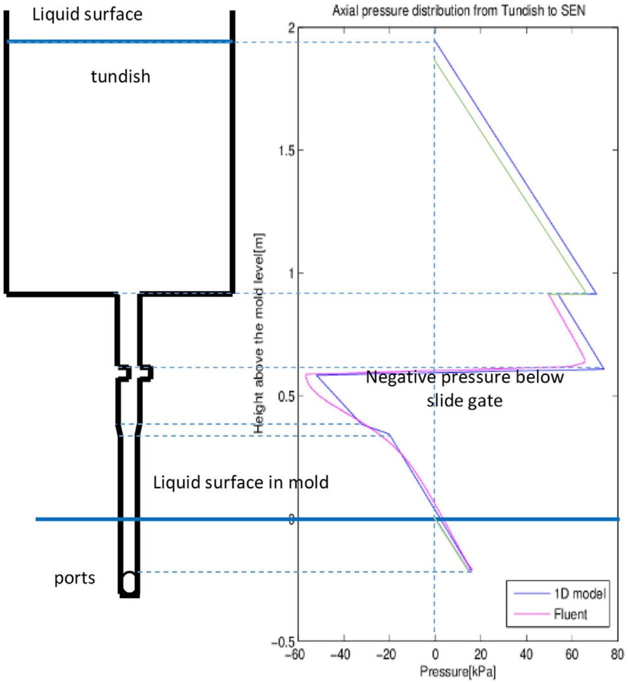

Figure 6. Pressure distribution down nozzle, comparing numerical, and analytical models.[100]

In order to determine the bubble size and flow-rate distribution that enters the steel, the gas flow distribution through the hot refractory has recently been modeled, including the effects of the refractory geometry, thermal expansion of the gas, temperature-dependent gas viscosity, and possible leakage into any unsealed joints. A one-way-flow pressure boundary condition was formulated and implemented to account for the pressure threshold needed to overcome surface tension to create a bubble at the refractory-steel interface, and to prevent unrealistic flow of steel into the refractory.[101]

The complete model was validated with both analytical solutions of 1-D test problems and observations of a water bubbling experiment, which is shown in Figure 7b and c.[101] For this particular nozzle geometry, note that no gas exits the lower left of the nozzle, owing to this pressure threshold. In the steel plant, both the pressure and flow rate of the gas are measured. Because this porous-flow model requires only one of these measurements as a boundary condition (the inlet pressure), the predicted flow rate can be compared with the measured flow rate, and the difference represents leakage.[101] Practical results suggest that the leakage can be significant, exceeding 50%.[49] This model could serve as an important initial step of a comprehensive multiphase model system.

3.5. Multiphase Fluid Flow in the Mold

Particle entrapment associated with flow problems in the mold is responsible for most of the serious defects in final-rolled

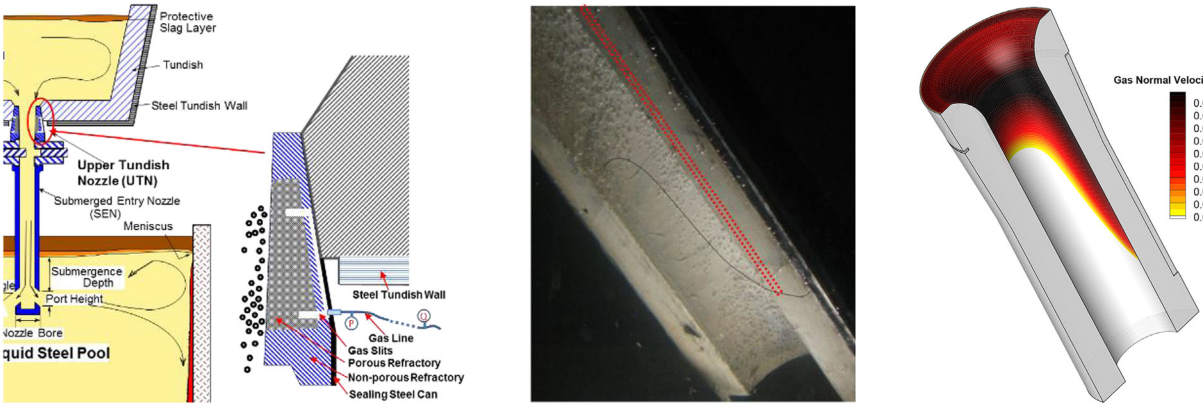

(a) (b) (c)

Figure 7. Comparison between predicted and measured gas flow rate at the upper tundish nozzle inner surface.[101] a) Schematic of gas injection process, b) Underwater experiment showing bubbling locations, c) Predicted gas normal surface velocity distribution. Reproduced with permission.[101] 2015, TMS.

continuous-cast products.[102] These include pinholes and blisters from entrapped bubbles, and the inclusions which often accompany them, especially in products with exposed (visible) surfaces, such as body panels for automotive and appliance applications. They also include slivers from inclusions and the entrainment of mold slag, which accompany flow problems in the mold, and are aggravated by unstable single-roll flow patterns, which is affected by the buoyancy of argon gas bubbles,[103] excessive surface velocity which can entrain the mold slag,[104] interactions with argon gas bubbles, leading to their eventual capture into the solidifying shell,[105] the capture of small inclusions by the argon bubbles, leading to surface defects such as slivers if they are captured, and surface level fluctuations that disrupt initial solidification in the meniscus region.[3,68] Each of these problems is associated with a different type of multiphase flow, which can be modeled via many different approaches.

Firstly, argon gas injection modifies the flow pattern, due to the two-way coupling between the bubbles and the turbulent flow field. The gas buoyancy lifts the jets exiting the nozzle ports, while the bubbles are dragged by the momentum of the turbulent flow. This has been the subject of many previous modeling studies,[58,60–64,66,69–88] using several different computational approaches. If the gas fraction is small, the most efficient method is a simple mixture model, such as Algebraic-Slip[66] or a modification.[69,70] These quasi-multiphase approaches include the effect of the bubbles via an extra source term in a single set of momentum equations for the fluid phase, and track the gas fraction by solving one extra transport equation. Results reveal that increasing Ar gas increases upward flow near the Submerged Entry Nozzle, (SEN) and tends to transform the classic double-roll flow pattern to a more detrimental single-roll flow pattern with surface flows directed away from the SEN toward the narrow faces.[70]

To improve on this by considering the bubble size distribution, Lagrangian methods, such as the Discrete Particle Method have been coupled together with the single set of fluid continuity and transport equations to track the trajectories of individual argon bubbles, and to include their local effects on the flow.[58,60,75,77,81,84] Using such an Eulerian–Lagrangian two-way coupled model of Ar-steel flow, with a $k-\varepsilon$ turbulence model, larger (0.25–2.5 mm diameter) bubbles were predicted to float directly upwards near the SEN to the top surface upon exiting the nozzle ports, while smaller ($<$0.25 mm) bubbles travel with the jet across the mold cavity.[81]

With higher gas fractions, it is more accurate to solve an extra continuity equation and complete extra set of transport equations for the gas phase, coupled together with the fluid continuity and transport equations, in order to enforce the total volume fraction to equal 100% everywhere. This Eulerian–Eulerian approach has been applied successfully in many previous studies of argon-steel flow in the continuous casting mold region.[56,61–64,66,71,72,76,78,80,82] Asymmetric, oscillating flow is observed if gas fractions are excessive.[62] Using a RANS $k-\varepsilon$ model for turbulence, parametric studies with this approach quantified how the detrimental transition from double-roll to single-roll could be avoided by keeping the argon gas volume fraction below a critical fraction, which is lower and easier to achieve with narrow mold width.[71]

The Eulerian–Eulerian approach has been extended to enable spatial variations in bubble size, and size evolution according to a population balance framework via the homogeneous MUlti-SIze Group (MUSIG) model.[106] Models of flow in continuous casting molds using this approach[73,74,87,88] match well with measurements of both flow pattern and bubble size in water models, except near to the SEN. Like DPM, the MUSIG method can correctly predict rising flow near the SEN that contains large bubbles and the steel jet that traverses directly across the mold cavity that transports smaller bubbles.[73,87,88] However, as with the Eulerian–Eulerian models, all bubble sizes in the homogeneous MUSIG model share a single gas velocity field, and momentum interactions with the fluid phase are governed by a local average bubble size.

To improve on these limitations, non-homogeneous MUSIG models have been developed recently, which enable each of the bubble size groups to have a different velocity field by solving more than one set of continuity and momentum equations for the gas phase.[85,86] Similar to other simpler multiphase models, results with this sophisticated method for handling bubbles show generally good agreement with measurements in water models, using the standard $k-\varepsilon$ model for turbulence.[85,86] All of these methods require the initial bubble size distribution to be input at the model inlets, so future work should be combined with output from the models of initial bubble size discussed in the previous section.

3.6. Level Fluctuations and Slag Entrainment

Another important aspect of flow in the mold is the profile of the top surface interface between the molten steel and the slag layers, and the fluctuations of this level. Excessive variations of the surface profile both in space (often called "standing wave"), and in time, (level fluctuations), lead to surface defects by upsetting the uniform infiltration of liquid slag into the gap between the shell and the mold, causing abnormal freezing of the meniscus to form hooks, the entrapment of mold slag, non-uniform heat transfer, and other problems. Excessive flow velocity across this slag-steel interface may lead to emulsification, vortexing, and the entrainment of slag droplets into the liquid pool. The simplest way to model surface profile variations from the results of a flow simulation with a fixed flat top surface is via a simple energy balance, converting the pressure variations into the potential energy of the level variations.[52,66,83,107] This method has been shown to be surprisingly accurate for many casting conditions.[52,54,58,66,83,107] because the relative height of the level variations is usually small. In this approach, it is easy to account for the molten steel displacing the slag layer, which can amplify the level changes.[52] However, this effect is usually small relative to simple rising and falling of the slag with level fluctuations, so the slag layer can be ignored when estimating level fluctuations.[58,83]

More advanced methods have been applied to simulate surface level and level fluctuations during continuous casting, including moving grid methods,[49,50,108–110] the free-surface Lattice–Boltzman method,[111] and the Volume of Fluid (VOF) method.[84,112–114] In addition to handling larger fluctuations accurately, these methods can capture the effects of surface tension and complex interactions between gravity and momentum forces, which can cause surface waves, sloshing, and slag entrainment. Simulations with VOF showed how surface instabilities move from the narrow face region to near the SEN with decreasing casting speed, owing to the decrease in dissipation of the jet momentum leaving the ports.[113,114] To understand the entrainment of slag droplets, starting from protrusions beneath the slag layer, entrainment has been modeled with VOF using LES on a fine grid and a special method to identify droplets, and found to match droplet sizes observed in a water model.[115] Using a moving grid method implemented into detached eddy simulations of the transient turbulent flow, dithering of the flow control device (e.g., stopper rod) at the wrong frequency was shown to cause severe surface sloshing instabilities, which matched predictions from an analytical model, and observations at the plant.[49,50] Using an Euler–Euler–Euler model for the molten steel, liquid slag, and air above the slag layer, and a Lagrangian DPM model for the argon gas particle transport, the behavior of four different phases was recently modeled.[116] This model showed how argon bubbles raise the slag-steel interface near the SEN, and cause more level fluctuations there, which matched well with physical model experiments of a slab caster where air bubbles were injected into water.[116]

3.7. Effect of Applied Electromagnetic Forces on Flow

In addition to nozzle geometry, strand cross section, casting speed, and argon injection, flow in the mold can be greatly affected by the application of electromagnetic forces. Computational models are ideal tools to investigate these effects and several important commercial configurations have been studied in slab casting, including with local,[117,118] single-ruler,[119–121] and double-ruler[54,58–60,72,107,122–124] ElectroMagnetic Braking (EMBr).

In the widely-used double-ruler configuration, or "FC-Mold", two rectangular-shaped magnetic fields are applied across the mold width, with one above and the other below the nozzle ports. Increasing the upper ruler strength tends to slow the surface velocities, decrease level profile variations, decrease level fluctuations, and dissipate high-frequency turbulent fluctuations inside the nozzle.[54,120,122,125] Increasing the strength of the lower ruler field tends to deflect the jet upwards, causing surface velocities and turbulence to increase.[54,122] Finding an optimal surface velocity and turbulence level is essential to avoid casting defects. Moving magnetic fields can create a stirring motion in the mold,[75,125–127] or can accelerate, or slow down the jets in the mold,[103,125] and are only recently receiving attention by modelers, owing to their complexity and the need for transient models.

It is important to include the effects of the conducting steel shell in the model, especially for transient simulations. This is because the current returning through the solid shell tends to stabilize the flow pattern and suppress unsteady low-frequency oscillatory behavior of the jets that occurs when the current returns through the fluid boundary layer, or Hartman layer. This effect on stability has been confirmed with both LES models[54,120,121] and with physical models using low-melting-temperature metal alloys.[128] Positioning a field directly across or in front of the ports should be avoided because this destabilizes the flow by amplifying minor variations in jet angle: slightly low jets are deflected downward and slightly upward jets are deflected upward.[129] The RANS approach cannot predict these transient phenomena.

The electromagnetic field is often combined with argon gas to alter flow in the mold. Computational models are better-suited than plant trials or lab experiments to study the complex interactions between these effects in commercial casters, and this important multiphysics problem is receiving more attention

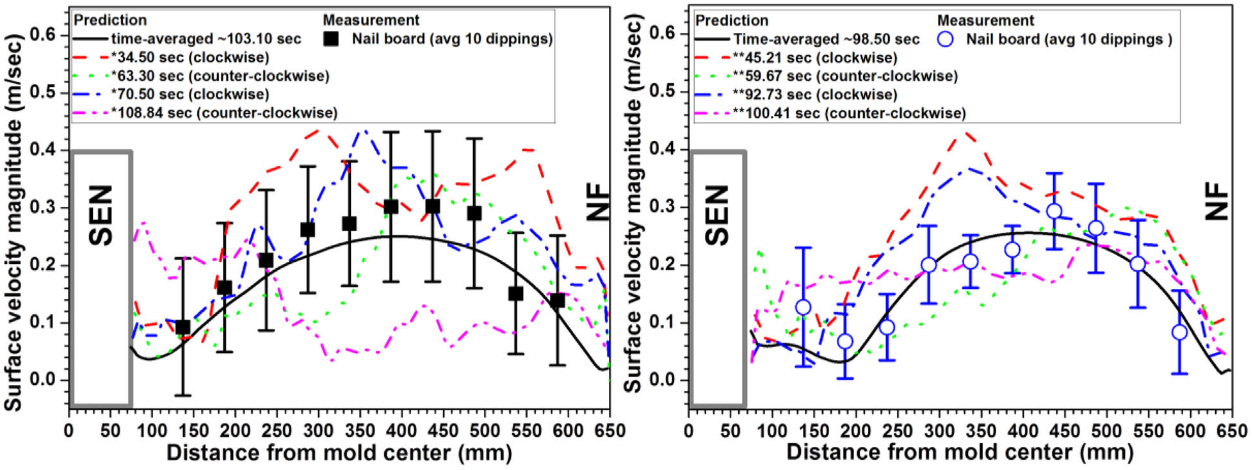

(a) (b)

Figure 8. Comparison of surface velocity variations between LES model predictions and measurements a) without and b) with EMBr. Reproduced with permission.[58] 2016, TMS.

in recent years.[58,60,72,75,130] Compensating for changing process conditions such as argon gas is difficult, however, so real-time measurement of the mold level profile and casting conditions combined with databases generated from computational-model results is being developed as a methodology for online control of the electromagnetic field to generate optimal mold flow conditions.[103]

Transient models can reveal deeper insights into the fundamental nature of the chaotic turbulent flow and electromagnetic effects. For example, **Figure 8** and **9** compare the surface velocities and level profiles measured in a typical slab caster with argon gas, both with and without double-ruler EMBr.[58] The LES model predictions agree well with nailbaord measurements in the operating caster. With EMBr, the surface velocity is slightly lower on average, and the level profile is flatter. Of greater importance, EMBr causes a significant decrease in the time variations of both surface velocity and level, which are indicated in the figure by the range of the predicted instantaneous profiles and the error bars on the measurements. A major cause of these fluctuations is revealed by LES results to

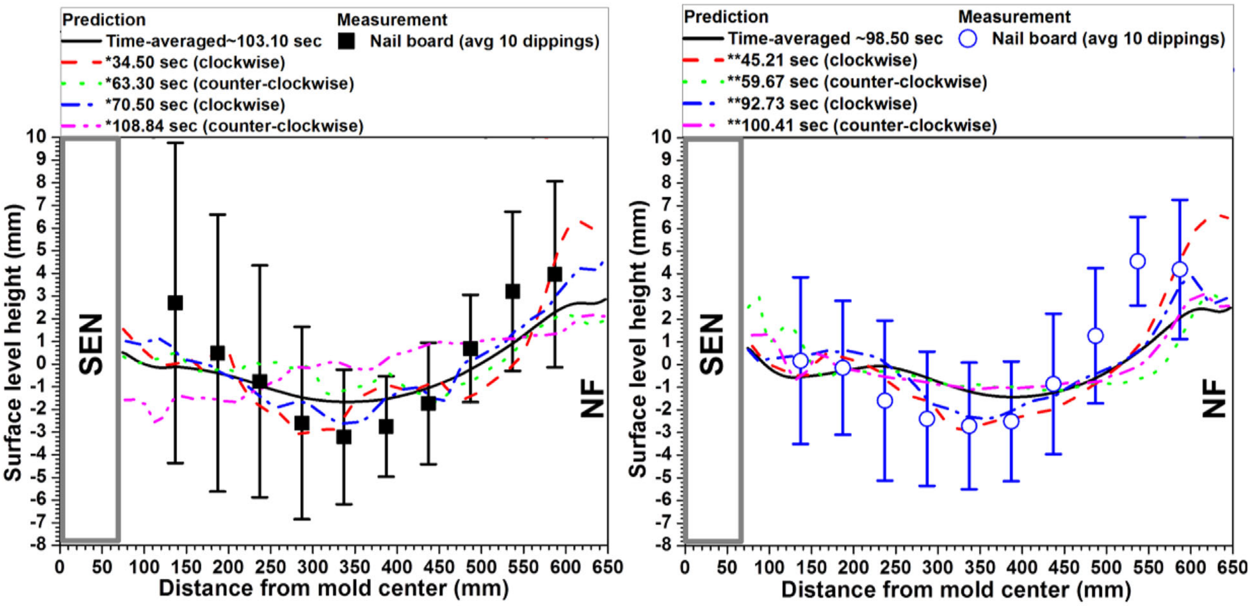

(a) (b)

Figure 9. Comparison of surface level variations between LES model predictions and measurements a) without and b) with EMBr. Reproduced with permission.[58] 2016, TMS.

be flipping between clockwise and counterclockwise flow exiting the nozzle ports. When flow from the slide gate opening, located toward the outside radius, goes straight down the outer-radius side of the nozzle, the jets exiting the ports swirl clockwise and are very strong, leading a short time later, (4.3 s) to a larger surface velocity with more level fluctuations. When flow from the slide gate bounces across to the inside-radius side of the nozzle, and thus exits the ports with a counter-clockwise swirl, some of its momentum is lost, the jets deflect more toward the outer radius of the mold, so the surface velocity a short time later is a little slower and the level fluctuations are smaller. The EMBr field of the upper ruler across the nozzle lessens the amount of flipping between swirl patterns exiting the ports, leading to more stable jet flow with less fluctuations in both surface velocity and level.[58]

Electromagnetic effects also have an important effect on particle capture, due to their influence on the general flow pattern, local turbulence, and boundary-layer flow. A few studies have investigated this, with both RANS models with random walk particle trajectories[118] and LES models.[60,123] The overall effect of EMBr on particle removal is small,[118] as most particles are small and easy to capture. By deflecting the jet upwards, EMBr can decrease the number of particles penetrating deep into the caster, thereby improving internal cleanliness.[118] However, this may increase particle capture high in the strand, which increases surface defects.[118] Depending on the EMBr orientation relative to the nozzle ports, sometimes the opposite occurs, due to EMBr deflecting the jet downward.[122] By generally increasing tangential velocity in the boundary layer, EMBr may lessen the capture of large particles by increasing the chances of bubbles and inclusions being washed off of the solidification front and back into the bulk flow. This is significant because the large bubbles and inclusions are of greatest concern to steel quality. More work is needed to validate and quantify these effects, coupling together the relevant phenomena in parametric studies of realistic caster geometries.

3.8. Superheat Transport

The transport of superheat by the turbulent fluid flow in the mold is very important to both initial solidification at the meniscus, where insufficient superheat can cause hook formation and surface defects, and final solidification, where excessive, nonuniform superheat distribution can change the solidification structure from equiaxed toward columnar, and aggravate centerline segregation. The superheat-temperature distribution is readily simulated by adding a simple energy transport equation to the fluid flow problem.[131,132]

These models show that most of the superheat is removed in the mold region, or just below.[131,132] As shown in **Figure 10**, the temperature decreases continuously with distance along the path travelled by the flowing jet, with the lowest temperatures found at the meniscus region, near the narrow faces and SEN, for a typical double-roll flow pattern.[132] Comparisons with plant measurements confirmed the model predictions that liquid in the upper recirculation zone above the jet in the mold cavity retains less than one third of its superheat temperature, as shown in **Figure 11**.[132]

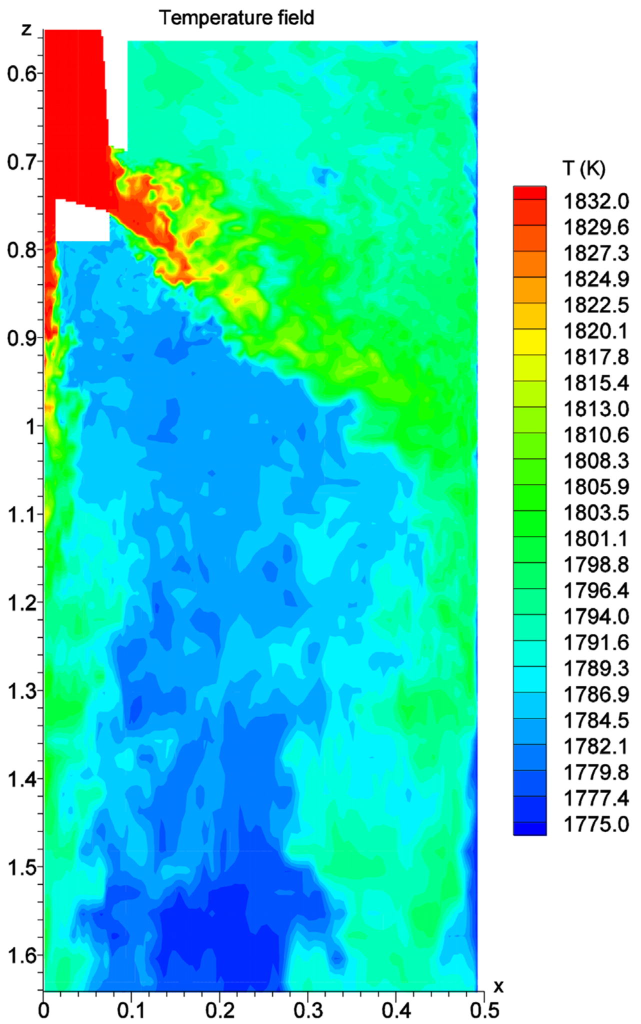

Figure 10. Instantaneous temperature calculated in centerplane with LES model. Reproduced with permission.[132] 2005, TMS.

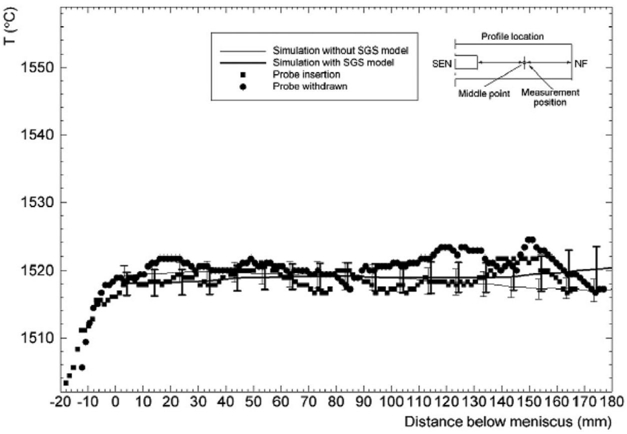

Figure 11. Comparison of temperature calculated down vertical line in mold with measurement from inserted probe. Reproduced with permission.[132] 2005, TMS.

The direction of the steel jets flowing from the nozzle controls the distribution of the superheat. If the nozzle port angle is directed too deep, then the critical meniscus region receives too little superheat, so the meniscus can solidify to form hooks, as discussed in the next section. In addition to its effect on hook formation and surface defects, superheat dissipation in the mold is also important to the formation and survival of crystal nuclei, which greatly influence microstructure development and segregation lower in the caster.

3.9. Thermal-Flow Models of Shell Solidification

Further coupling the fluid flow and energy transport model with solidification enables direct study of how the superheat transported by the flowing molten steel affects shell growth. The numerical methodologies to couple these phenomena together efficiently have been pioneered by Beckermann, Voller, and coworkers.[133–135] Rather than solving for temperature directly, many thermal-flow models with solidification solve for enthalpy, with subsequent lookup of temperature, in order to achieve better numerical stability. The tremendous changes in thermal and flow properties from liquid to solid are often handled with temperature- and/or phase- dependent properties. The large effective viscosity of the solid is often achieved by simply fixing the solid velocity to the casting speed.

Together with an accurate model of heat transfer across the interfacial gap between the solidifying steel and the mold or secondary-cooling chamber, a computational thermal-fluid flow model can predict the shape of the solidifying steel shell, including the local shell-thinning effect near the point of jet impingement onto the solidification front, for example at the narrow face in a slab caster,[79] or inner shoulder in a beam-blank caster.[34,136] To accurately capture this behavior requires a very refined mesh, however, in order to avoid exaggeration of the effect of the fluid flow on the shell growth.[79] Heat transfer calculations are more sensitive to achieving adequate grid refinement in the boundary layers than are velocity calculations.[21,132] In addition, careful attention should the paid to choosing the terms in the transport equations so that the latent heat released during columnar solidification into the solid should not be advected away with the flow.[79] This differs from the solidification of equiaxed grains, which many models are based upon.

Other recent thermal-flow models with solidification showed that the flow pattern in the mold, as affected by electromagnetic braking, had a significant effect on the solidification profile, which extended all the way to the shape of the final solidification front, or "crater end" that defines the metallurgical length.[137] This crater-end shape has an important effect on centerline defects, and was found to exhibit a W-shape profile across the strand width, with deeper fluid penetration near the microstructure triple-points, caused by downward flow along the narrow faces, together with stronger surface heat removal from the water sprays along the strand centerline.[137,138]

3.10. Particle Entrapment

Steel quality is greatly determined by the entrapment of inclusions during continuous casting in the mold region, which originate from upstream, the entrainment of slag from the top surface of the mold, or from the entrapment of argon gas bubbles coated with inclusions. Many computational models have been applied in recent years to simulate particle transport and entrapment into the solidifying steel shell, starting with a RANS or LES model of turbulent flow, and then solving a simple one-way coupled Lagrangian DPM method to track the particle motion.[53,57,60,77,79,81,85,118,123,130,139–141]

To predict the capture of particles, including both inclusions and small gas bubbles, a suitable capture criterion is needed. The simple criterion that particles are entrapped if they touch the solidification front is often used. This is a reasonable approximation for particles smaller than the primary dendrite arm spacing.[140] However, small particles might flow into the mushy zone, navigate between the dendrites, and escape back into the bulk flow. This can be modeled by including solidification heat transfer into the fluid-flow model, but this computationally-intensive approach also needs a very fine mesh to resolve the mushy region[79] and empirical fitting parameter(s), in order to match with plant measurements.[142]

Larger particles are more difficult to capture, and require a more advanced capture criterion. Because it cannot fit between the dendrites, a large particle touching the solidification front can be stopped, surrounded by dendrites that grow around it, and captured, only if the tangential drag forces from the flowing fluid that try to rotate it away are insufficient to overcome a force balance with the other forces acting on the particle. In addition to drag, lift, virtual mass, pressure-gradient, and buoyancy/gravity forces, which also affect particle transport in the bulk flow, additional forces acting in the boundary layer include the lubrication, Van der Waals, and surface tension gradient forces.[79,140] Surface tension gradients are caused by solute rejection at the solidification front, which produces concentration gradients in highly-segregating, surface-active elements. This lowers the surface tension near the solidification front, which generates a force toward the solidification front that increases particle capture in steel grades rich in elements such as S[140] or Ti.[103] More research is needed to study these phenomena with validated, quantitative models.

With a steady RANS flow model, the chaotic motion of the turbulent particle trajectories can be approximated using the Random Walk method, which adds a random velocity component to the particle velocity, that is, proportional to the local turbulence level.[57,77,79,81,85,94,118,130,140,142] Unfortunately, this method assumes isotropic turbulence, which near solid walls or the solidification front, over-estimates the local velocity component toward those boundaries. This likely explains why this method has been observed to overestimate particle capture, relative to plant measurements.[142]

A more accurate method is to simulate the chaotic motion of the particles directly, using a transient Large Eddy Simulation for the turbulent fluid flow.[53,60,123,140,141] **Figure 12** shows that captured small particles are widely distributed.[60] These results for bubble capture match reasonably well with plant

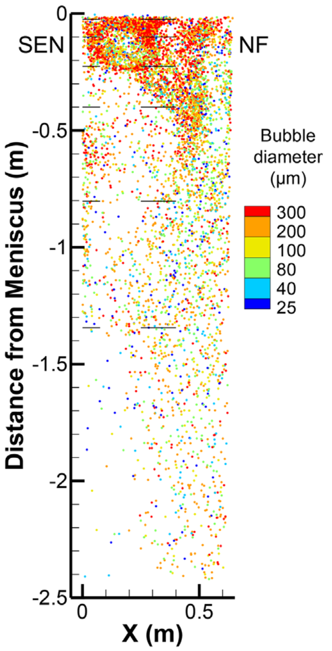

Figure 12. Location of small bubbles captured on wideface with advanced criterion. Reproduced with permission.[130] 2016, TMS.

measurements of capture fraction and distribution in the solidified slab, and also with particle size distribution, as shown in **Figure 13**. [60] Note that this model underpredicts particle capture near the meniscus, which end up near the strand surface, perhaps due to its neglect of entrapment by solidified hooks and/or its assumption of complete removal into the slag layer of every particle that touches the top surface.

Using flow fields obtained from both RANS and LES simulations, most of the small inclusions (92% of those $<40\,\mu m$[53] and 85% of those $<80\,\mu m$[130]) are found to be entrapped in the final product, as shown in **Figure 14**. Gas injection increases the removal rate (average number of inclusions removed per unit time) of small particles to the top surface slag layer.[140] Using an advanced capture criterion, only a very small fraction ($<0.02\%$) of larger bubbles (>1 mm) are captured (Figure 14).[130] The simple capture criterion greatly overpredicts the capture of large particles. Also, to achieve reproducible results, (removal rate variations within $\pm3\%$), more than 2500 particles of each size should be tracked.[140]

The attachment of inclusions to bubbles, while they are being transported through the molten steel pool is another important phenomenon, which fundamental models of individual bubbles can help to understand. One such study found that bubbles circulating in the mold can entrap many small inclusions, even though the chances of any given inclusion becoming attached to the bubble is small.[143] Smaller bubbles are more efficient at inclusion attachment and removal for a given gas volume, so long as they are not captured into solidifying shell.[143] Another model recently confirmed this finding and further quantified the important contribution of the wake behind the bubble.[144] Future modeling studies of turbulent flow, transport, and capture of particles should combine more of these phenomena together.

4. Initial Solidification at the Meniscus

The initial solidification of the tip of the steel shell at the meniscus around the perimeter of the continuous-casting mold is of paramount importance because it creates the surface of the final product. The behavior of this region is governed by very complex interrelated phenomena during each oscillation cycle. Recent advanced computational models focus either on thermal-fluid flow behavior in the region or on thermal stress in the solidifying steel shell. To capture all of the known behaviors realistically would require combining both model types together into a true multiphysics model, which is beyond current capabilities.

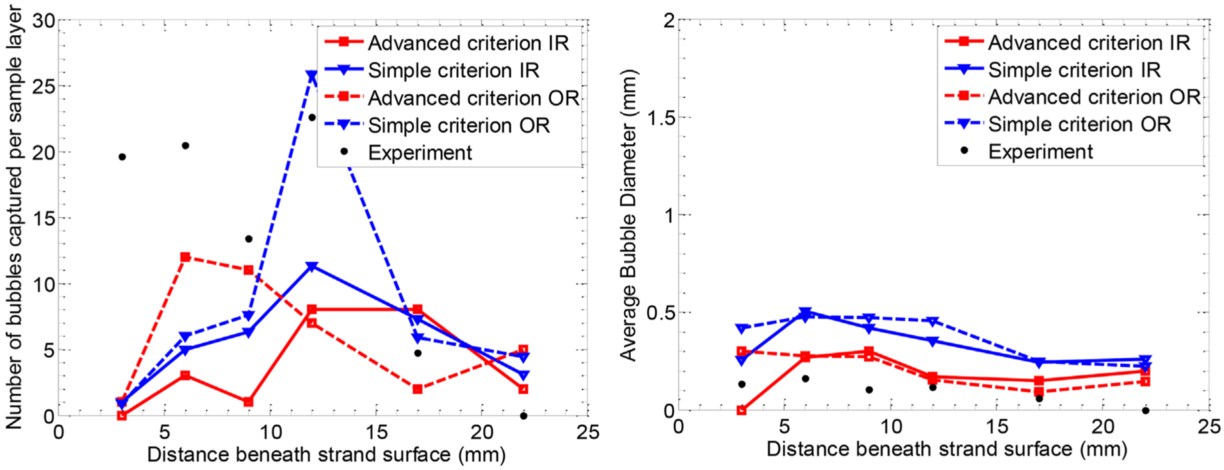

Figure 13. Number of bubbles captured on each layer of center sample (left) and corresponding average diameter (right),[130] where OR is outer radius and IR is inner radius. Reproduced with permission.[130] 2016, TMS.

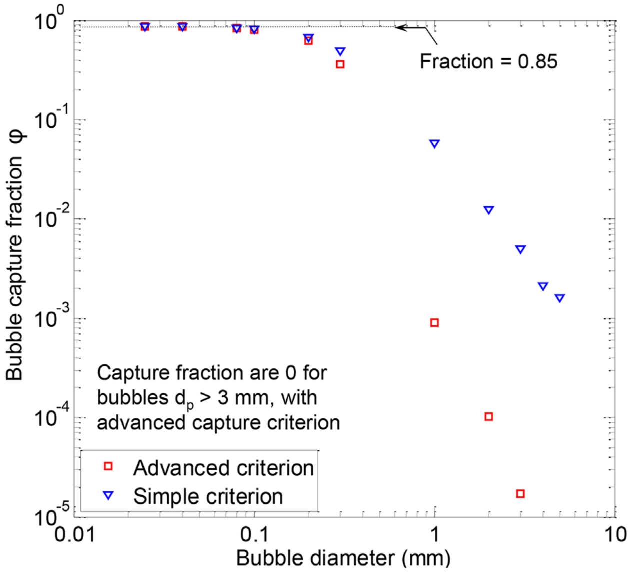

Figure 14. Fraction of bubbles captured for varying bubble diameter. Reproduced with permission.[130] 2016, TMS.

4.1. Thermal-Fluid-Based Meniscus Models

Advanced thermal-fluid models of the meniscus region,[2,38,39,145–149] solve the transient heat conduction equation in the mold, interfacial gap, solid and molten steel, and slag. Transient fluid flow in the molten steel and slag is modeled with a set of momentum equations, mass conservation, phase fractions of the slag and steel, and the VOF method to resolve the changing shape of both the meniscus and interfacial gap that separates the slag and steel. Transient flow must properly include turbulence in the molten steel bulk that diminishes to laminar flow toward the boundary layer near the solidification front, which can be handled by k–ω Shear-Stress Transport (SST) models[39,149] or by LES.

Mold powder added to the top surface in the mold heats, sinters, melts, and flows down to form a molten slag layer that floats on the molten steel. The increase in thermal conductivity, initial increase in viscosity during sintering, and subsequent drop in viscosity during melting, are modeled via temperature-dependent property functions.[38,39,149] Slag in this liquid layer moves slowly and intermittently toward the meniscus region, where some solidifies against the oscillating mold wall to form a rigid rim that pushes down on the meniscus during each downstroke. Some slag is pushed down to be consumed into the interfacial gap where it cools, may crystalize, or may undergo a glass transition, and some is dragged down by the moving solid steel shell that is imposed to move downward at the casting speed. This requires a different set of temperature-dependent properties for the cooling slag near the mold walls and in the interfacial gap.[38,39,149]

Temperature-dependent properties are also required in the steel phase, including the great increase in viscosity (by >10 orders of magnitude)[39] that accompanies solidification from liquid to solid. This creates computationally difficulty, which can be handled by assuming the solid steel is rigid.[38,39,149]

Typical results for the changes in temperature, velocity, and phase fraction contours during an oscillation cycle are shown in **Figure 15**a.[149] A very fine mesh, 50 micron cell spacing in this example,[149] is needed to capture the large gradients in properties and field variables that occur over the short distances involved. The shell tip, which forms the bottom of the eventual oscillation mark, moves steadily downward with time. This stretches the meniscus downwards until the ferrostatic pressure of the molten steel can no longer be supported by the surface tension, and the meniscus overflows the shell tip, during Figure 15a frames d–f. This creates a small “hook”, where the partly solidified meniscus extends into the molten steel. These hooks are often observed near the strand surface in micrographs such as Figure 15b, and are detrimental because they can capture bubbles and inclusions, leading to surface defects.[150] This also completes formation of the surface oscillation mark, which moves down at the casting speed, and essentially retains its shape in the final slab. This particular simulation was run for >8 oscillation marks. The pitch between oscillation marks, their depth and shape, and the variations in these parameters for this and several similar simulations all match reasonably well with plant measurements and their variations.[39,149] Some of these variations are rooted in the classic chaotic behavior of complex systems.[148] Predicted slag consumption rates and trends with operating parameters also agree well with measurements.[38,39]

Temperature evolution at different locations in the mold wall can be compared with thermocouple measurements for model validation.[38,39] Comparison with average heat flux based on heat-up of the cooling water is also useful for validation of heat flux profiles for runs which extend to mold exit. These models can also predict tangential shear stress evolution along the mold wall,[39,149] which potentially could be compared with mold friction measurements in future work. Improved insight into the relationship between defect formation and real-time measured parameters such as heat transfer and friction could enable better online diagnostic tools to benefit commercial operations.

4.2. Thermal-Mechanical-Based Meniscus Models

Another approach to model initial solidification at the meniscus is to use a thermal-stress model, which is needed, for example, to understand the well-known important effects of steel grade on oscillation mark and crack formation. A few thermal-mechanical models of the initial solidifying shell have been developed[150–155] and applied to study distortion behavior during level fluctuations,[151] the effect of steel grade,[11,152,154] and initial cracks.[155] These models, together with measurements, have revealed new insight into the mechanism of hook formation,[150] which build on the overflow mechanism illustrated by the thermal-fluid model results in Figure 15a. In addition to overflow, thermal distortion can contribute to the shape of the lower (downstream) surface of the oscillation mark.[150] Although mechanical distortion of the liquid meniscus during oscillation is of critical importance to oscillation mark formation and slag consumption, mechanical bending of the solidified meniscus hook is unlikely, because it is so strong and brittle.[150] Ultralow carbon steels and peritectic steel grades experience the greatest thermal distortion, and consequently the deepest oscillation marks, both in the

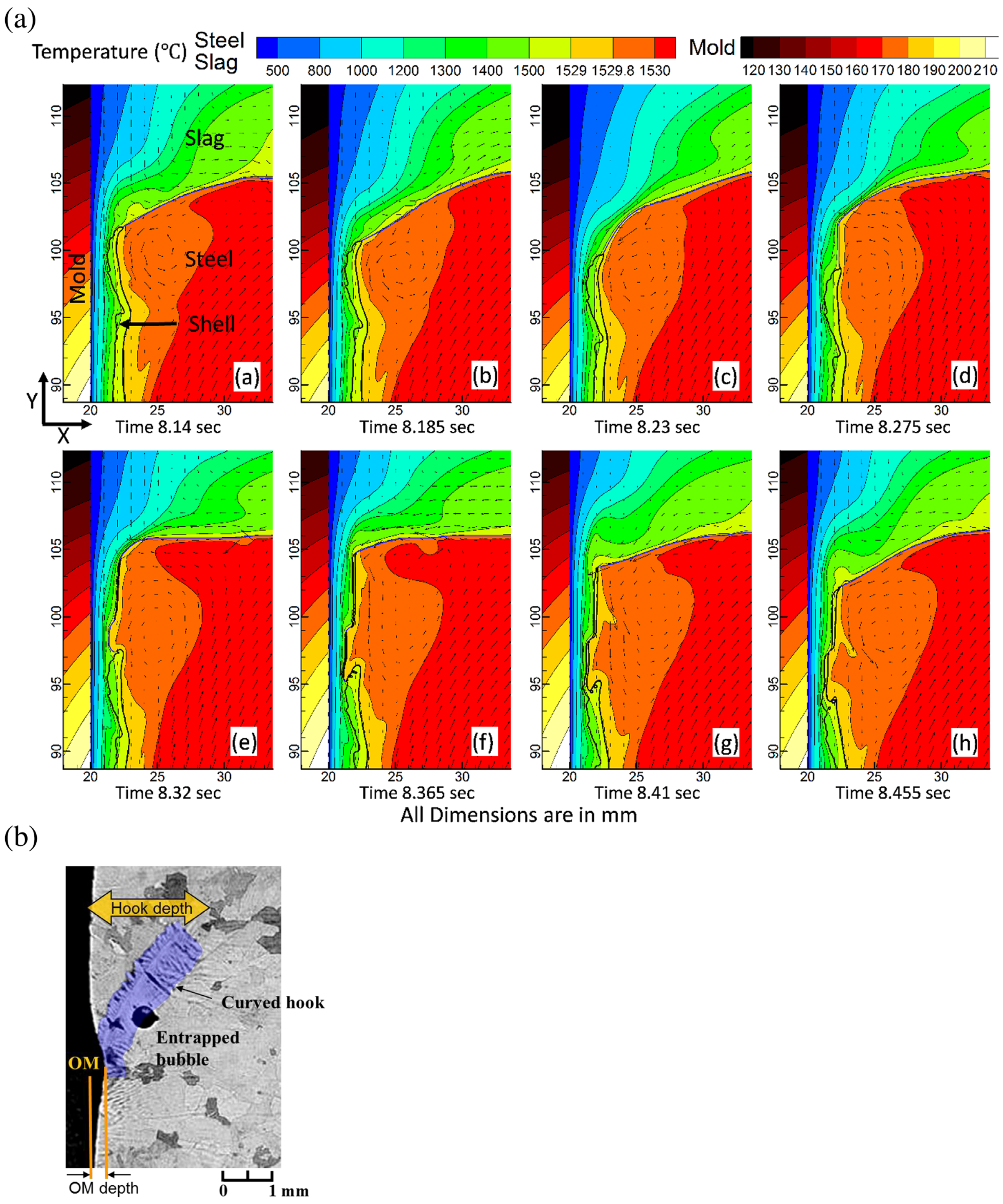

Figure 15. a) Thermal-fluid model of meniscus region behavior during an oscillation cycle, showing shape of meniscus and solidified steel shell outlined in black.[149] b) Photograph of an as-cast microstructure cross section, showing a typical oscillation mark with a hook. Reproduced with permission.[150] 2006, TMS.

model simulations and experiments.[152,154] This is because these steels have more phase-transformation shrinkage from delta to austenite in the solid state, while the solid steel shell is both strong enough to resist ferrostatic pressure and thin enough to experience significant thermal distortion.[152,154] The next sections discuss thermal-mechanical models in more detail.

5. Thermal-Mechanical Behavior of the Mold

Thermal distortion of the mold from startup to steady operation is important to residual stress, residual distortion, fatigue cracks, and life of the mold, which in turn can greatly affect steel quality.[9,156] Mold distortion is also important to heat transfer and mechanical behavior of the solidifying shell, due to its great effect on the interfacial gap between the mold and shell, and is a critical consideration in the design of mold taper.[33,157] Mold thermal distortion has been explored with computational thermal-stress models for steady casting conditions in square billet molds,[157,158] round billet molds,[17,30,33] conventional thick-slab molds,[19,20,159] beam-blank molds,[160] and in thin-slab molds with [9,156,161,162] and without[9,161] a funnel. Each mold shape has distinctive thermomechanical behavior. These studies have revealed the importance of not oversimplifying the geometry, applying appropriate contact constraints between connecting parts,[159,162] and using appropriate loading conditions and material constitutive equations,[161] in order to simulate reasonable thermal-mechanical behavior of the system.

To simulate thermal distortion of the mold and its related phenomena first requires solving the heat conduction equation, typically using measurements to help determine the interfacial heat flux needed to obtain an accurate temperature field. In addition, a thermal-mechanical model must solve the equilibrium equations which relate force and stress, the constitutive equations which relate stress and strain, and the compatibility equations which relate strain and displacement. Thermal strain is calculated from the temperature solution. Three-dimensional finite-element models, including plasticity and creep if desired, can be developed using commercial finite-element packages such as ABAQUS,[163] which are well-suited to this nonlinear thermal stress problem. Details are given elsewhere.[161,162]

In order to accurately simulate the thermal-mechanical behavior and match the measured distortion, models should include all important geometric features of the mold, which for a typical slab mold includes four copper plates with their water slots,[159] a reinforced steel water box assembly,[159] and tightened bolts.[162] Its four-piece construction causes a slab mold to behave very differently from single-piece billet and bloom molds.

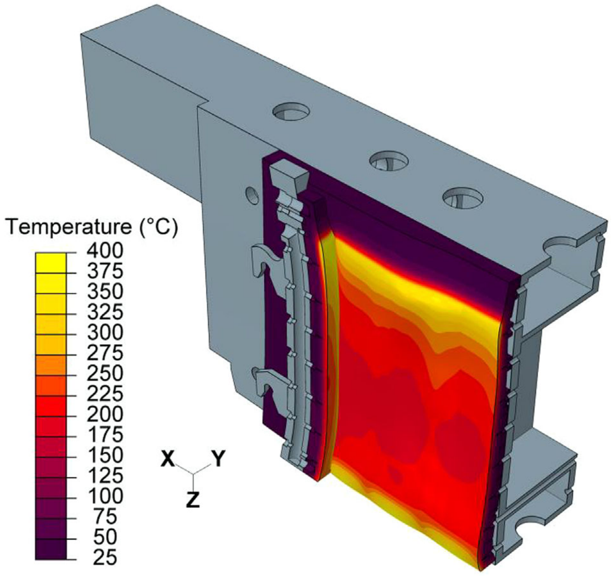

Figure 16. Temperature field simulated in a thin-slab casting mold with thermal distortion (magnified 50×). Reproduced with permission.[162] 2012, TMS.

Figure 16 shows example temperature contours and the displaced shape calculated in one quarter of a commercial thin-slab funnel-mold caster under steady operating conditions.[162] The hot exterior of each copper plate attempts to expand, but is constrained by its colder interior and the constraint of the cold, steel water box which is attached to it. This makes each plate bend inwards toward the solidifying steel, typically on the order of one millimeter as observed on the narrow face in this mold. The wideface distortion of this particular mold is very different, however, owing to its waterbox being hollowed out to house an electromagnetic breaking system, so the shorter bolts going through just the backing plate pull the copper plates back toward the central region of the wideface. Thus, the maximum inward distortion on the wideface is predicted near the location of highest temperature just below the meniscus and another distortion peak is found near the mold bottom.

The thermal expansion causes the narrow face to distort into a trapezoidal shape that contacts the wide face along just a thin vertical line at the front corner of its hot face. This thin edge must transmit all of the clamping forces, so is susceptible to accelerated wear, especially during automatic width changes. If clamping is too high, the hot edge can be crushed, causing a gap after cooling, which can lead to finning defects or even a sticker breakout, if steel enters that gap during startup. In addition, the widefaces may be scratched, leading to longitudinal cracks, and other defects on the strand surface.

Another problem is permanent distortion and crack formation in the mold surface, especially in the meniscus region where temperature is highest. Constraining the thermal expansion induces compressive stress and creep in the hot face of the copper plates. This compression relaxes during operation, which leads to residual tensile stress after cooling. Repeated cycles can build up significant distortion of the mold plates and fatigue cracks.[9] Their removal requires increased remachining and reduces mold life.[9]

Transient thermal-mechanical behavior of the mold has received much less attention. One recent modeling study investigated the behavior of this same thin-slab mold during a startup.[96] **Figure 17** and **18** show how the liquid level, position of the mold bottom being withdrawn downward by the dummy bar, and thermal distortion all evolve with time.[96] The predictions in Figure 18 are compared with two sets of inclinometer measurements obtained during startup and during operation, which confirm both the inward-curved shape of the mold narrow-faces and the magnitude of the distortion.[96] These distortion

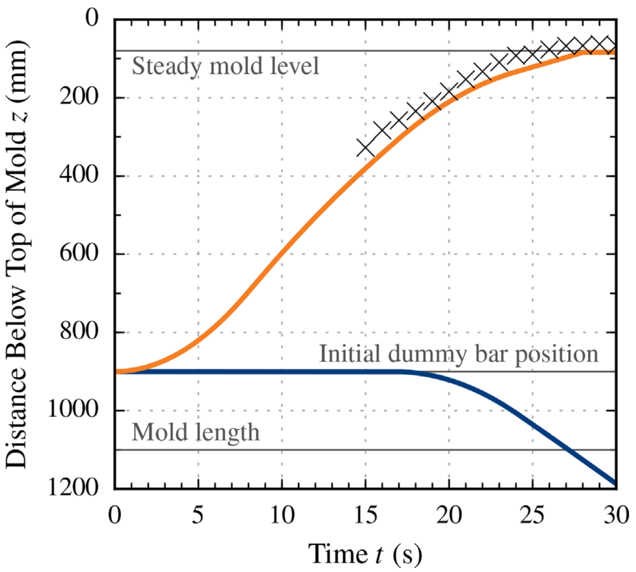

Figure 17. Mold level and dummy bar positions during startup.[96] 2014, ASMET.

predictions are important for designing mold taper to avoid detrimental air gap formation, especially for new mold designs.

6. Thermal-Mechanical Modeling

Thermal-mechanical models are needed to investigate many important phenomena in steel continuous casting. Examples include gap formation and crack formation in the mold, bulging between rolls, bending and unbending, the formation of surface depressions, and internal cracks, and segregation. In solving the same equations needed for mold distortion, the total strain is divided into elastic, thermal, and inelastic components, the latter needed to handle plasticity and creep in the solidifying steel.

Because the liquid level at the top free surface in the mold is free to rise and fall, the mass contained in the computational domain for the mechanical analysis can change with time during the process, and it is usually too expensive to include this free surface in the model domain. This issue can be addressed in several other ways, such as by introducing another strain component for the fluid flow,[164] leaving space for shrinkage in the central portion of the domain,[34,164,165] or by adopting an Arbitrary Lagrangian–Eulerian (ALE) formulation, where the internal fluid flow region is solved with an Eulerian methodology and the exterior mechanical behavior of the moving solid shell is solved with a Lagrangian method.[166]

Modeling the constitutive behavior of the solid steel is difficult, owing in part to the challenge in finding accurate experimental measurements of thermal-mechanical properties at the high temperatures (including solidification), low strains, (less than 2%), and low strain rates (10^{-6} to $10^{-2}\,s^{-1}$) relevant to this casting process. The problem is further complicated by the growing number of different steel grades of commercial importance, such as advanced high-strength steels, which have very different thermal-mechanical properties. A promising approach to simplify the problem of conducting mechanical tests on so many different grades is to consider that the mechanical properties are governed mainly by the phases present.[11,167–170] Delta-ferrite is much softer and prone to creep than austenite.[168,169] The effect of steel grade on stress generation during initial solidification has recently been studied using such a phase-dependent constitutive-model approach.[11]

Accurate computational modeling requires verification with known analytical solutions followed by comparison with plant measurements. Unlike models of heat transfer and fluid flow, where such validation has become routine, it is much less common to see proper verification and validation of thermal-mechanical models prior to their application to practical continuous casting problems. An excellent analytical solution of solidification of an elastic-perfectly-plastic material exists,[171] which has been used for verification of a few thermal-mechanical models of steel continuous casting.[11,34,35,164,165] These studies

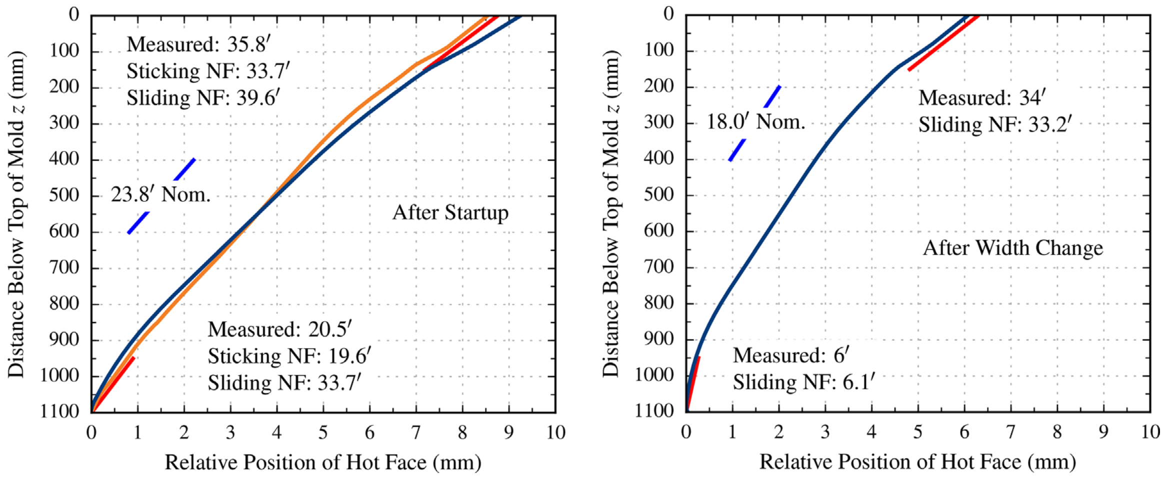

Figure 18. Simulated narrow face mold shape (curved lines) and inclinometer measurements (straight lines) just after startup and after a width change.[96] 2014, ASMET.

reveal that achieving mesh refinement is still an obstacle to accurate modeling, as a much finer mesh is needed for mechanical analysis than for thermal modeling alone. Comparison of thermal-mechanical model predictions with stress measurements is rare. A few models have successfully matched lab measurements of temperature and force evolution in solidifying steel specimens including the submerged split-chill contraction test[172] and the gleeble test.[173] Direct plant measurements of stress during continuous casting are more difficult.

6.1. Surface Shape Problems

Surface shape problems that have been studied with thermal-mechanical computational models include deep oscillation marks and transverse depressions,[151,154] longitudinal depressions,[165,174] off-corner gutters,[174] rhomboidity in square billets,[175] ovalization of round billets,[35,176] and bulging in large blooms and slabs.[3,166,177,178] Unless they are extreme, the shape problems themselves are less important than the cracks and macrosegregation problems that often accompany them. Predicting surface shape is an easier first step for models to tackle, however, and comparison with plant measurements is easier as well.

In the mold, the shape of the shell governs the gap size and heat transfer in the corner region, and depends on how well the taper profile of the thermally-distorted mold balances the shrinkage, considering that ferrostatic pressure and creep both act to minimize gap formation. Insufficient taper leads to excessive gap formation, locally-decreased heat transfer, higher shell temperatures, recrystallization, strain concentration, and crack formation. Excessive taper is equally problematic, as it can cause the shell either to jam in the mold leading to transverse cracks, or to buckle, leading to longitudinal depressions inside the mold, which can grow below the mold, and form subsurface cracks. Thermal-mechanical models are an excellent tool to investigate such problems, and to optimize mold taper.[37,174] Coupling them with a detailed model of the interfacial gap model enables better accuracy in the corner regions, by accounting for phenomena such as a larger local air gap decreasing heat transfer across the gap, resulting in lower mold temperature, hotter shell surface temperatures, and a thinner shell.[15,31,35–37,179]

Even better accuracy can be achieved if the effects of fluid flow are taken into account by coupling with a thermal-flow model. A few models have demonstrated such multiphysics approaches, which are especially important in the mold, where flow has a large influence on shell growth.[36,37,179] Thermal distortion of the mold should be taken into account as well, which further complicates the multiphysics model.[34]

Below the mold, excessive bulging between the rolls, such as caused by either ferrostatic pressure with a large roll pitch or misaligned rolls, can cause subsurface transverse cracks, called radial streaks, and contribute to centerline macrosegregation. Many models have simulated this steady bulging problem.[3,166,177,178] Even more problematic is transient bulging, which causes the volume of the entire internal liquid pool to change with time.[180] This periodic or chaotic squeezing of the shell leads to corresponding liquid level fluctuations at the meniscus region in the mold, causing surface defects if the level control system is unable to overcome the problem. This dynamic bulging problem is receiving attention recently with thermal-mechanical models.[181] Similar models are being applied to study the effects of taper of the machine below the mold: in particular, the process of soft reduction to mitigate centerline problems.[27,182,183]

6.2. Crack Formation

Crack formation has plagued the continuous casting process since its inception, and limits the steel grades that a particular caster can produce. Severe cracks are responsible for catastrophic breakouts. Because strains are always small during the casting process, cracks only arise when local tensile stresses are accompanied by severe metallurgical embrittlement. Thus, crack modeling typically involves evaluating the results of a macroscale thermomechanical model using a failure criterion.

Most cracks in continuous-casting are caused by hot tearing, which has been characterized by empirical cracking criteria,[170,184–187] that involve a critical level of strain accumulation over a critical temperature range near final solidification, and depends on steel composition and strain rate. A few recent studies have evaluated the accuracy of different hot tearing criteria by modeling lab experiments, which deform a solidifying steel ingot.[170,186,188] Specific types of hot-tear crack defects have been the focus of several successful modeling studies in continuous casting of steel,[35,176,189] The microstructure greatly affects hot tearing, as columnar structures that predominate just beneath the strand surface are more susceptible than equiaxed structures, but models rarely include this.[35,170] On the microscale, models are just beginning to tackle the detailed hot tearing phenomenon that involves steel dendrites pulling apart when interdendritic fluid flow is too constrained. As discussed later, this remains a modeling challenge.

Some cracks, such as transverse cracks, which typically open up during bending or unbending of the strand, are due mainly to intermediate-temperature embrittlement, due to strain concentration at the austenite grain boundaries, made worse when many small precipitates are present. These cracks occur at much higher local strains and depend even more strongly on the microstructure, so have received less attention by modelers. These cracks especially would benefit from microstructure modeling, focusing on solid-state transformations and grain-boundary embrittlement.

7. Segregation

Macrosegregation is one of the most serious defects in continuous-cast steel. Unlike internal cracks, voids, and porosity, which are greatly improved by the subsequent rolling process, the related problem of macrosegregation cannot be removed and always ends up in the final product. Modeling of macrosegregation is extremely difficult because it requires an accurate thermal-solidification model of the caster, modeling of microsegregation between dendrites which generates the solute, macroscale fluid flow which redistributes the solute, volumetric thermal shrinkage, and mechanical deformation which induce the flow, and finally failure of the microstructure, which accumulates the solute locally into a defect. Many models of microsegregation at the local scale between secondary dendrite arms have been developed for steel, and match reasonably well with measurements, although more work is needed for complicated multicomponent alloys, especially peritectic steels.[190,191]

Although significant progress has been made since a review of the modeling challenges over a decade ago,[192] macrosegregation modeling is still in its infancy. Most macrosegregation models have adopted a thermal-fluids modeling approach, solving mass and momentum transport equations for the fluid, combined with conservation and transport equations for the solute, and including methodologies to handle the transport and removal of latent heat, the phase transformation from liquid to solid, movement of the solid, and a microsegregation model.[193–195] Both liquid and solid are assumed incompressible.

A few macrosegregation models have been applied to simulate fluid flow, solute transport, and segregation in the mold region, to predict macrosegregation at the strand surface. One recent model simulated the effect of electromagnetic stirring on turbulent fluid flow, superheat transport, free-surface motion, temperature, solidification, and solute distribution in a continuous bloom-casting mold with a bifurcated nozzle.[127] The stirring increased top surface level fluctuations, but also caused faster removal of mold superheat, leading to a thinner shell in the mold, and a slight segregation profile, with negative segregation (less alloy) at the shell surface, which was roughly the same trend as measurements of carbon content made near the bloom surface.

Other thermal-fluid-solute models have focused on centerline segregation that develops lower in the caster, and include a model to prescribe bulging between the support rolls and mechanical soft reduction.[193–195] The results show strong positive segregation at the strand centerline, with nearby regions of negative segregation.

One multiphysics model used an ALE approach to simulate the fluid flow, solute transport, and mechanical deformation of the solidifying shell and predicted both the bulging between rolls during secondary cooling, and the resulting macrosegregation near the centerline.[166] Other models are needed to include electromagnetics. More work is needed on quantitative validation of macrosegregation models in continuous casting. Furthermore, the important effects on solute transport of the columnar and equiaxed microstructure, including its local deformation and failure, remain a challenge for macrosegregation models to include in the future.

8. Microstructure

Modeling microstructure during steel solidification is important to augment the macroscale modeling of continuous casting, especially in the prediction of defects such as cracks and segregation. The task of detailed simulation of microstructure formation is daunting, however, as the evolving columnar-equiaxed dendritic structure depends on all time and length scales of the entire caster, and involves three dimensions. Moreover, it depends heavily on the evolving temperature field, fluid flow, solute flow, complex phase transformations in multicomponent alloys, mechanical stress and strain, and segregation.

In recent years, a few models have started to simulate dendrite formation in steel, using cellular automata[196,197] or phase-field methods.[198–200] Applications include the prediction of the columnar to equiaxed transition,[196] secondary dendrite arm spacing,[197] the delta to austenite massive-like phase transformation,[200] fracture strength during solidification,[198] and how alloys affect hot tearing.[199] Difficulties include finding material properties, such as interface energies, which depend on the models used to extract them, and the huge computational resources needed for fine-grid 3D domains of sufficient size. Thus, empirically-based models are very useful alternatives for microstructure parameters such as dendrite arm spacing and grain size.[21] In conclusion, microstructure modeling deserves more attention in the context of continuous casting of steel, to contribute to other models and/or to commercial practice.

9. Conclusions

Significant progress has been made in the ability of computational models to accurately predict fundamental phenomena in the continuous casting process (nozzle, mold, and strand), including temperature, solidified shell growth, turbulent fluid flow together with multiphase phenomena, electromagnetic effects and particle transport, microstructure and grain structure, thermal-mechanical behavior, distortion, and stress. Indeed, basic heat transfer models are being used as part of model-based online control systems, for the control of spray water flow rates and breakout-detection warning systems in the commercial process. Significant inroads are being made toward predictions under transient conditions, which are often when defects form. However, the accurate prediction of real defects that affect the cast product is still in its infancy. Model predictions of clogging, inclusion entrapment, segregation, and cracks need much further validation and testing. Finally, the coupling together of the different phenomena into multiphysics models, including the vastly different length and time scales of interest will remain a challenge.

On the bright side, the increasing power of computer hardware and modeling software has enabled significant advances, leading to models that incorporate many of the important fundamental phenomena that are relevant to solving practical problems. Validation of heat transfer and fluid-flow models with plant measurements is routine, and progress is being made on all aspects of the challenges mentioned above. Future advances to the real commercial processes will require intelligent combination of all tools available: plant experiments, physical modeling, laboratory experiments, and increasingly: computational modeling.

Acknowledgements

The author thanks the member companies of the Continuous Casting Center at the Colorado School of Mines and the National Science Foundation Grant CMMI 15-63553 for funding to make this work possible.

Thanks are also extended to Hyunjin Yang for help with the multiphase flow references.

Conflict of Interest

The author declares no conflict of interest.

Keywords

computational models, continuous casting, fluid flow, heat transfer, review, solidification, steel, stress analysis, validation

Received: July 23, 2017
Revised: October 22, 2017

[1] *World Steel in Figures 2016*; World Steel Association, worldsteel.org: **2016**, p. 1.
[2] K. C. Mills, P. Ramirez-Lopez, P. D. Lee, B. Santillana, B. G. Thomas, R. Morales, *Ironmaking Steelmaking* **2014**, *41*, 242.
[3] B. G. Thomas, *Metall. Mater. Trans. B* **2002**, *33*, 795.
[4] V. R. Voller, C. R. Swaminathan, B. G. Thomas, *Int. J. Numer. Methods Eng.* **1990**, *30*, 875.
[5] V. R. Voller, *Adv. Numer. Heat Transfer* **1997**, *1*, 341.
[6] J. E. Lait, J. K. Brimacombe, F. Weinberg, *Ironmaking Steelmaking* **1974**, *1*, 90.
[7] R. B. Mahapatra, J. K. Brimacombe, I. V. Samarasekera, N. Walker, E. A. Paterson, J. D. Young, *Metall. Trans. B* **1991**, *22B*, 861.
[8] C. A. M. Pinheiro, I. V. Samarasekera, J. K. Brimacombe, B. N. Walker, *Ironmaking Steelmaking* **2000**, *27*, 37.
[9] J.-K. Park, B. G. Thomas, I. V. Samarasekera, U.-S. Yoon, *Metall. Mater. Trans. B* **2002**, *33B*, 437.
[10] B. Petrus, K. Zheng, X. Zhou, B. G. Thomas, J. Bentsman, *Metall. Mater. Trans. B* **2011**, *42*, 87.
[11] M. L. S. Zappulla, B. G. Thomas, L. C. Hibbeler, *Metall. Mater. Trans. A* **2017**, *48A*, 3777.
[12] J. Yang, Z. Xie, J. Ning, W. H. Liu, Z. P. Ji, *Metall. Mater. Trans. B* **2014**, *45*, 1545.
[13] Y. Meng, B. G. Thomas, *ISIJ Int.* **2006**, *46*, 660.
[14] J. Sengupta, M. Trinh, D. Currey, B. G. Thomas, in *AISTech 2009 Steelmaking Conf. Proc.*, Louis, MO **2009**.
[15] J. X. Song, Z. Z. Cai, F. Y. Piao, M. Y. Zhu, *J. Iron Steel Res. Int.* **2014**, *21*, 1.
[16] X. D. Wang, L. W. Kong, M. Yao, X. B. Zhang, *Metall. Mater. Trans. B* **2017**, *48*, 357.
[17] J. Lee, H. Han, K. Oh, J. Yoon, *ISIJ Int.* **1999**, *39*, 435.
[18] X. D. Liu, M. Y. Zhu, *ISIJ Int.* **2006**, *46*, 1652.
[19] F. M. Du, X. D. Wang, Y. Liu, T. Y. Li, M. Yao, *J. Iron Steel Res. Int.* **2016**, *23*, 83.
[20] X. Liu, M. Zhu, *ISIJ. Int.* **2006**, *46*, 1652.
[21] V. K. De Barcellos, V. L. D. Gschwenter, H. Kytonen, C. A. Dos Santos, J. A. Spim, S. Louhenkilpi, J. Miettinen, *Steel Res. Int.* **2010**, *81*, 461.
[22] Y. Meng, B. G. Thomas, *Metall. Mater. Trans. B* **2003**, *34*, 685.
[23] L. C. Hibbeler, M. M. C. See, J. Iwasaki, K. E. Swartz, R. J. O'malley, B. G. Thomas, *Appl. Math. Model.* **2016**, *40*, 8530.
[24] B. Petrus, D. Hammon, M. Miller, B. Williams, A. Zewe, Z. Chen, J. Bentsman, B. G. Thomas, *Iron Steel Technol.* **2015**, *12*, 58.
[25] M. J. Long, D. F. Chen, Q. X. Wang, D. H. Luo, Z. W. Han, Q. Liu, W. X. Gao, *Ironmaking Steelmaking* **2012**, *39*, 370.
[26] J. Yang, Z. Xie, Z. P. Ji, H. J. Meng, *ISIJ Int.* **2014**, *54*, 328.
[27] C. Ji, C. H. Wu, M. Y. Zhu, *JOM* **2016**, *68*, 3107.
[28] H. H. An, Y. P. Bao, M. Wang, L. H. Zhao, *Metall. Res. Technol.* **2017**, *114*, 405.
[29] Z. W. Han, D. F. Chen, K. Feng, M. J. Long, *ISIJ Int.* **2010**, *50*, 1637.
[30] J. E. Kelly, K. P. Michalek, T. G. Oconnor, B. G. Thomas, J. A. Dantzig, *Metall. Trans. A* **1988**, *19*, 2589.
[31] B. G. Thomas, A. Moitra, R. Mcdavid, *Iron Steelmaker (ISS Trans)* **1996**, *23*, 57.
[32] Y. Meng, B. G. Thomas, *Metall. Mater. Trans. B* **2003**, *34*, 707.
[33] Y. Hebi, Y. Man, Z. Huiying, F. Dacheng, *ISIJ Int.* **2006**, *46*, 546.
[34] S. Koric, L. C. Hibbeler, R. Liu, B. G. Thomas, *Numer. Heat Transfer B-Fundam.* **2010**, *58*, 371.
[35] M. R. Ridolfi, S. Fraschetti, A. De Vito, L. A. Ferro, *Metall. Mater. Trans. B* **2010**, *41*, 1293.
[36] M. Y. Zhu, Z. Z. Cai, H. Q. Yu, *J. Iron Steel Res. Int.* **2013**, *20*, 6.
[37] Z. Z. Cai, M. Y. Zhu, *ISIJ Int.* **2013**, *53*, 1818.
[38] A. S. M. Jonayat, B. G. Thomas, *Metall. Mater. Trans. B* **2014**, *45*, 1842.
[39] C. Blaes, *MS Thesis*, Colorado School of Mines, **2017**.
[40] M. Jauhola, E. Livela, J. Konttinen, E. Laitinen, S. Louhenkilpi, *Steel Transl.* **1995**, *25*, 19.
[41] R. A. Hardin, K. Liu, A. Kapoor, C. Beckermann, *Metall. Mater. Trans. B* **2003**, *34*, 297.
[42] A.-G. Hou, Q.-L. Zhang, G.-D. Xu, M.-F. Jiang, *J. Iron Steel Res. Int.* **2015**, *22*, 98.
[43] B. G. Thomas, L. F. Zhang, *ISIJ Int.* **2001**, *41*, 1181.
[44] Q. Yuan, B. Zhao, S. P. Vanka, B. G. Thomas, *Steel Res. Int.* **2005**, *76*, 33.
[45] Ansys Fluent Theory Guide, *Release 16.2.* Ansys Inc., Canonsburg, PA, www.ansys.com: **2016**.
[46] B. E. Launder, D. B. Spalding, *Comput. Methods Appl. Mech. Eng.* **1974**, *13*, 269.
[47] R. Chaudhary, C. Ji, B. G. Thomas, S. P. Vanka, *Metall. Mater. Trans. B* **2011**, *42*, 987.
[48] C. Kratzsch, K. Timmel, S. Eckert, R. Schwarze, *Steel Res. Int.* **2015**, *86*, 400.
[49] R. Liu, *PhD Thesis*, University of Illinois at Urbana-Champaign, **2014**.
[50] R. Liu, B. G. Thomas, L. Kalra, T. Bhattacharya, A. Dasgupta, *Iron Steel Technol.* **2014**, *11*, 87.
[51] K. Jin, S. P. Vanka, R. K. Agarwal, B. G. Thomas, *Int. J. Comput. Fluid D* **2017**, *31*, 36.
[52] Q. Yuan, B. G. Thomas, S. P. Vanka, *Metall. Mater. Trans. B* **2004**, *35*, 685.
[53] Q. Yuan, B. G. Thomas, S. P. Vanka, *Metall. Mater. Trans. B* **2004**, *35*, 703.
[54] R. Singh, B. G. Thomas, S. P. Vanka, *Metall. Mater. Trans. B* **2014**, *45*, 1098.
[55] B. K. Li, Z. Q. Liu, F. S. Qi, F. Wang, G. D. Xu, *Acta Metall. Sin.* **2012**, *48*, 23.
[56] Z. Q. Liu, B. K. Li, M. F. Jiang, L. Zhang, G. D. Xu, *Acta Metall. Sin.* **2013**, *49*, 513.
[57] Z. Liu, B. Li, M. Jiang, *Metall. Mater. Trans. B* **2014**, *45*, 675.
[58] S. M. Cho, B. G. Thomas, S. H. Kim, *Metall. Mater. Trans. B* **2016**, *47*, 3080.
[59] K. Jin, S. P. Vanka, B. G. Thomas, *Metall. Mater. Trans. B* **2017**, *48*, 162.
[60] K. Jin, S. P. Vanka, B. G. Thomas, *Metall. Mater. Trans. B* **2017**, (under revision) in press.
[61] Z. Liu, B. Li, *Metall. Mater. Trans. B* **2017**, *48*, 1833.
[62] H. Bai, B. G. Thomas, *Metall. Mater. Trans. B* **2001**, *32*, 253.
[63] H. Bai, B. G. Thomas, *Metall. Mater. Trans. B* **2001**, *32*, 269.

[64] H. Bai, B. G. Thomas, *Metall. Mater. Trans. B* **2001**, *32*, 707.
[65] R. Chaudhary, G. G. Lee, B. G. Thomas, S. M. Cho, S. H. Kim, O. D. Kwon, *Metall. Mater. Trans. B* **2011**, *42*, 300.
[66] R. Liu, B. G. Thomas, J. Sengupta, S. D. Chung, M. Trinh, *ISIJ Int.* **2014**, *54*, 2314.
[67] L. L. Zhang, D. F. Chen, M. J. Long, H. B. Chen, Y. W. Huang, Z. H. Dong, *Metals-Basel* **2016**, *6*, 104.
[68] B. G. Thomas, in *Making, Shaping and Treating of Steel: Continuous Casting*, 11 edn., AISE Steel Foundation, Pittsburgh, PA **2003**, p. 14.1.
[69] N. Bessho, R. Yoda, H. Yamasaki, T. Fujii, T. Nozaki, S. Takatori, *ISIJ Int.* **1991**, *31*, 40.
[70] B. G. Thomas, X. Huang, R. C. Sussman, *Metall. Mater. Trans. B* **1994**, *25*, 527.
[71] D. Creech, *M.S. Thesis*, University of Illinois at Urbana-Champaign, Urbana, IL, **1999**.
[72] B. Li, T. Okane, T. Umeda, *Metall. Mater. Trans. B* **2000**, *31*, 1491.
[73] T. Shi, *M.S. Thesis*, University of Illinois at Urbana-Champaign, Urbana, IL, **2001**.
[74] Q. Yuan, T. Shi, S. P. Vanka, B. G. Thomas, in *Computational Modeling of Materials, Minerals and Metals Processing*, TMS, Warrendale, PA **2001**, p. 491.
[75] T. Toh, H. Hasegawa, H. Harada, *ISIJ Int.* **2001**, *41*, 1245.
[76] R. Sánchez-Pérez, L. García-Demedices, J. P. Ramos, M. Díaz-Cruz, R. D. Morales, *Metall. Mater. Trans. B* **2004**, *35*, 85.
[77] C. Pfeiler, M. Wu, A. Ludwig, *Metall. Mater. Trans. A* **2005**, *413*, 115.
[78] V. Singh, S. K. Dash, J. S. Sunitha, S. K. Ajmani, A. K. Das, *ISIJ Int.* **2006**, *46*, 210.
[79] C. Pfeiler, B. G. Thomas, M. Wu, A. Ludwig, A. Kharicha, *Steel Res. Int.* **2008**, *79*, 599.
[80] Z. Q. Liu, B. K. Li, M. F. Jiang, F. Tsukihashi, *ISIJ Int.* **2013**, *53*, 484.
[81] C. L. Liu, Z. G. Luo, T. Zhang, S. Deng, N. Wang, Z. S. Zou, *J. Iron Steel Res. Int.* **2014**, *21*, 403.
[82] Z. Q. Liu, F. S. Qi, B. K. Li, M. F. Jiang, *J. Iron Steel Res. Int.* **2014**, *21*, 1081.
[83] S. M. Cho, S. H. Kim, B. G. Thomas, *ISIJ Int.* **2014**, *54*, 845.
[84] P. E. Ramirez-Lopez, P. N. Jalali, J. Björkvall, U. Sjöström, C. Nilsson, *ISIJ Int.* **2014**, *54*, 342.
[85] Z. Liu, F. Qi, B. Li, M. Jiang, *Metall. Mater. Trans. B* **2015**, *46*, 933.
[86] Z. Liu, L. Li, F. Qi, B. Li, M. Jiang, F. Tsukihashi, *Metall. Mater. Trans. B* **2015**, *46*, 406.
[87] L. M. Li, Z. Q. Liu, B. K. Li, *J. Iron Steel Res. Int.* **2015**, *22*, 30.
[88] Z. Q. Liu, F. S. Qi, B. K. Li, S. C. P. Cheung, *Int. J. Multiphase Flow* **2016**, *79*, 190.
[89] H. Bai, B. G. Thomas, *Metall. Mater. Trans. B* **2001**, *32*, 1143.
[90] K. G. Rackers, B. G. Thomas, in *Continuous Casting Vol. 10 Tundish Operations*, Iron Steel Society, Warrendale, PA **2003**, p. 264.
[91] S. Z. Wu, J. M. Zhang, Z. Z. Li, *J. Iron Steel Res. Int.* **2010**, *17*, 6.
[92] E. Gutierrez, S. Garcia-Hernandez, J. D. J. Barreto, *Steel Res. Int.* **2016**, *87*, 1406.
[93] J. Knoepke, M. Hubbard, J. Kelly, R. Kittridge, J. Lucas, in *Steelmaking Conf. Proc.*, Iron Steel Society, Chicago, IL **1994**, p. 381.
[94] B. G. Thomas, A. Dennisov, H. Bai, in *80th Steelmaking Conference Proc.*, Iron and Steel Society (AIST), Warrendale, PA **1997**, p. 375.
[95] M. Long, X. Zuo, L. Zhang, D. Chen, *ISIJ Int.* **2010**, *50*, 712.
[96] L. C. Hibbeler, B. G. Thomas, R. C. Schimmel, H. H. Visser, in *ECCC2014*, ASMET, Leoben, Austria **2014**, p. 675.
[97] R. B. Tuttle, J. D. Smith, K. D. Peaslee, *Metall. Mater. Trans. B* **2007**, *38*, 101.
[98] L. Wang, C. Beckermann, *Metall. Mater. Trans. B* **2006**, *37*, 571.
[99] F. M. White, *Fluid Mechanics*, 7 edn., McGraw Hill, International **2011**.
[100] H. Yang, B. G. Thomas, "Mathematical Models of Continuous Casting of Steel Slabs", BG Thomas, ed., Annual Report to Continuous Casting Consortium, University of Illinois, August 19, 2015.Mathematical Models of Continuous Casting of Steel Slabs", BG Thomas, ed., Annual Report to Continuous Casting Consortium, University of Illinois, August 19, 2015
[101] R. Liu, B. G. Thomas, *Metall. Mater. Trans. B* **2015**, *46*, 388.
[102] J. Herbertson, Q. L. He, P. J. Flint, R. B. Mahapatra, in *Steelmaking Conf. Proc.*, Iron Steel Society (AIST), Washington, D.C. **1991**, p. 171.
[103] P. H. Dauby, *Rev. Metall.* **2012**, *109*, 113.
[104] J. Kubota, K. Okimoto, A. Shirayama, H. Murakami, in *Mold Operation for Quality and Productivity*, Iron Steel Soc (AIST), **1991**.
[105] S. Feldbauer, A. Cramb, in *PTD Conf. Proc.*, Iron Steel Soc. (AIST), Warrendale, PA **1995**, p. 327.
[106] S. M. Lo, *Application of Population Balance to CFD Modeling of Bubbly Flow via the MUSIG Model*, AEAT-1096, AEA Technology, Canonsburg, PA **1996**.
[107] Y.-S. Hwang, P.-R. Cha, H.-S. Nam, K.-H. Moon, J.-K. Yoon, *ISIJ Int.* **1997**, *37*, 659.
[108] A. Theodorakakos, G. Bergeles, *Metall. Trans. B* **1998**, *29*, 1321.
[109] G. A. Panaras, A. Theodorakakos, G. Bergeles, *Metall. Mater. Trans. B* **1998**, *29*, 1117.
[110] B. Rietow, B. G. Thomas, in *AISTech 2008*, Assoc. Iron Steel Tech., Warrendale, PA Pittsburgh, PA **2008**.
[111] P. Zhao, Q. Li, S. B. Kuang, Z. S. Zou, *Metall. Mater. Trans. B* **2017**, *48*, 456.
[112] Y. Wang, L. Zhang, *ISIJ Int.* **2010**, *50*, 1777.
[113] P. Ramírez-López, L. G. Demedices, O. Dávila, R. Sánchez-Pérez, R. D. Morales, *Metall. Mater. Trans. B* **2005**, *36*, 787.
[114] I. Calderon-Ramos, R. D. Morales, *Metall. Mater. Trans. B* **2016**, *47*, 1866.
[115] P. Zhao, Q. Li, S. B. Kuang, Z. S. Zou, *High Temp. Mater. Proc.-Isr.* **2017**, *36*, 551.
[116] Z. Q. Liu, Z. B. Sun, B. K. Li, *Metall. Mater. Trans. B* **2017**, *48*, 1248.
[117] K. Cukierski, B. G. Thomas, *Metall. Mater. Trans. B* **2008**, *39*, 94.
[118] Y. F. Wang, L. F. Zhang, *Metall. Mater. Trans. B* **2011**, *42*, 1319.
[119] X. C. Miao, K. Timmel, D. Lucas, Z. M. Ren, S. Eckert, G. Gerbeth, *Metall. Mater. Trans. B* **2012**, *43*, 954.
[120] R. Chaudhary, B. G. Thomas, S. P. Vanka, *Metall. Mater. Trans. B* **2012**, *43*, 532.
[121] R. Singh, B. G. Thomas, S. P. Vanka, *Metall. Mater. Trans. B* **2013**, *44*, 1201.
[122] S. M. Cho, S. H. Kim, B. G. Thomas, *ISIJ Int.* **2014**, *54*, 855.
[123] Z. Q. Liu, L. M. Li, B. K. Li, *JOM* **2016**, *68*, 2180.
[124] K. Jin, S. P. Vanka, B. G. Thomas, *TMS Annual Meeting*, Nashville, TN, **2016**, p. 159.
[125] E. Takeuchi, M. Zeze, T. Toh, S. Mizoguchi, *Magnetohydrodynamics Proc. Met*, Szekely, J., Ed. TMS, Warrendale, PA **1991**.
[126] A. Maurya, P. K. Jha, *Appl. Math. Model.* **2017**, *48*, 736.
[127] Q. Fang, H. W. Ni, B. Wang, H. Zhang, F. Ye, *Metals-Basel* **2017**, *7*, 72.
[128] K. Timmel, S. Eckert, G. Gerbeth, *Metall. Mater. Trans. B* **2011**, *42*, 68.
[129] B. G. Thomas, R. Singh, S. P. Vanka, K. Timmel, S. Eckert, G. Gerbeth, *J. Manuf. Sci. Prod.* **2015**, *15*, 93.
[130] K. Jin, B. G. Thomas, X. M. Ruan, *Metall. Mater. Trans. B* **2016**, *47*, 548.
[131] X. Huang, B. G. Thomas, F. M. Najjar, *Metall. Trans. B* **1992**, *23*, 339.
[132] B. Zhao, B. G. Thomas, S. P. Vanka, R. J. O'malley, *Metall. Mater. Trans. B* **2005**, *36B*, 801.
[133] J. Ni, C. Beckermann, *Metall. Trans. B* **1991**, *22*, 349.
[134] C. Y. Wang, C. Beckermann, *Metall. Mater. Trans. A* **1996**, *27*, 2754.
[135] V. R. Voller, C. Prakash, *Int. J. Heat Mass Tranfer* **1987**, *30*, 1709.
[136] L. L. Zhang, D. F. Chen, H. B. Chen, M. J. Long, X. Xie, *Ironmaking Steelmaking* **2017**, *44*, 193.

[137] Q. Q. Wang, L. F. Zhang, *JOM* **2016**, *68*, 2170.
[138] M. J. Long, D. F. Chen, L. F. Zhang, Y. Zhao, Q. Liu, *Met. Int.* **2011**, *16*, 19.
[139] Y. F. Wang, A. P. Dong, L. F. Zhang, *Steel Res. Int.* **2011**, *82*, 428.
[140] B. G. Thomas, Q. Yuan, S. Mahmood, R. Liu, R. Chaudhary, *Metall. Mater. Trans. B* **2014**, *45*, 22.
[141] Z. Q. Liu, L. M. Li, B. K. Li, M. F. Jiang, *JOM* **2014**, *66*, 1184.
[142] L. Zhang, Y. F. Wang, *JOM* **2012**, *64*, 1063.
[143] L. Zhang, J. Aoki, B. G. Thomas, *Metall. Mater. Trans. B* **2006**, *37*, 361.
[144] Y. G. Xu, M. Ersson, P. G. Jonsson, *ISIJ Int.* **2016**, *56*, 1982.
[145] P. E. Ramirez-Lopez, P. D. Lee, K. C. Mills, *ISIJ Int.* **2010**, *50*, 425.
[146] P. E. Ramirez-Lopez, P. D. Lee, K. C. Mills, B. Santillana, *ISIJ Int.* **2010**, *50*, 1797.
[147] P. E. Ramirez-Lopez, K. C. Mills, P. D. Lee, B. Santillana, *Metall. Mater. Trans. B* **2012**, *43*, 109.
[148] P. D. Lee, P. E. Ramirez-Lopez, K. C. Mills, B. Santillana, *Ironmaking Steelmaking* **2012**, *39*, 244.
[149] X. Yan, A. Jonayat, B. G. Thomas, in *TMS Annual Meeting, Frontiers in Solidification*, TMS, Nashville, TN **2016**, p. 181.
[150] J. Sengupta, B. G. Thomas, H. J. Shin, G. G. Lee, S. H. Kim, *Metall. Mater. Trans. A* **2006**, *37A*, 1597.
[151] B. G. Thomas, H. Zhu, in *Proceedings of Internat. Symposia on Advanced Materials & Tech. for 21st Century*, Ohnaka, I., Stefanescu, D., Eds. TMS, Warrendale, PA: Honolulu, HI, **1996**, pp 197–208.
[152] B. G. Thomas, J. T. Parkman, in *Solidification* **1998**, *1998*, 509.
[152] B. G. Thomas, J. T. Parkman, in *Solidification* **1998**, *1998*, 509.
[153] C. Ojeda, J. Sengupta, B. G. Thomas, J. Barco, J. Arana, *Luis in AISTech 2006 Steelmaking Conf. Proc.*, AIST, Warrendale, PA **2006**, p. 1017.
[154] J. Sengupta, C. Ojeda, B. G. Thomas, *Int. J. Cast Met. Res.* **2009**, *22*, 8.
[155] X. J. Zuo, R. G. Lin, N. Wang, J. Yang, X. N. Meng, M. Y. Zhu, *Steel Res. Int.* **2016**, *87*, 413.
[156] T. O'conner, J. Dantzig, *Metall. Mater. Trans. B*. **1994**, *25B*, 443.
[157] I. V. Samarasekera, D. L. Anderson, J. K. Brimacombe, *Metall. Trans. B* **1982**, *13*, 91.
[158] I. V. Samarasekera, J. K. Brimacombe, *Ironmaking Steelmaking* **1982**, *9*, 1.
[159] B. G. Thomas, G. Li, A. Moitra, D. Habing, *I&SM (ISS Trans.)* **1998**, *25*, 125.
[160] L. C. Hibbeler, S. Koric, K. Zhu, B. G. Thomas, C. Spangler, *Iron Steel Technol*. **2008**, *6*, 60.
[161] J.-K. Park, B. G. Thomas, I. V. Samarasekera, U.-S. Yoon, *Metall. Mater. Trans. B* **2002**, *33B*, 425.
[162] L. C. Hibbeler, B. G. Thomas, R. C. Schimmel, G. Abbel, *Metall. Mater. Trans. B* **2012**, *43*, 1156.
[163] Abaqus, *Standard User Manuals v6.4*. Abaqus, Inc.: Providence, RI **2004**.
[164] C. Li, B. G. Thomas, *Metall. Mater. Trans. B* **2004**, *35*, 1151.
[165] L. C. Hibbeler, B. G. Thomas, B. Santillana, A. Hamoen, A. Kamperman, *Metall. Ital*. **2009**, 29.
[166] V. D. Fachinotti, S. Le Corre, N. Triolet, M. Bobadilla, M. Bellet, *Int. J. Numer. Methods Eng*. **2006**, *67*, 1341.
[167] C. L. Zhang, M. Bellet, M. Bobadilla, H. F. Shen, B. C. Liu, *Acta Metall. Sin*. **2010**, *46*, 1206.
[168] P. F. Kozlowski, B. G. Thomas, J. A. Azzi, W. Hao, *Metall. Trans. A* **1992**, *23*, 903.
[169] S. Koric, B. G. Thomas, *J. Manuf. Proc. Technol*. **2008**, *197*, 408.
[170] M. R. Ridolfi, *Metall. Mater. Trans. B* **2014**, *45*, 1425.
[171] J. H. Weiner, B. A. Boley, *J. Mech. Phys. Solids* **1963**, *11*, 145.
[172] M. Rowan, B. G. Thomas, R. Pierer, C. Bernhard, *Metall. Mater. Trans. B* **2011**, *42*, 837.
[173] C. L. Zhang, M. Bellet, M. Bobadilla, H. F. Shen, B. C. Liu, *Metall. Mater. Trans. A* **2010**, *41A*, 2304.
[174] B. G. Thomas, A. Moitra, R. McDavid, in *Continuous Casting*, Iron Steel Soc, (AIST), Warrendale, PA **1997**, p. 337.
[175] S. Kumar, J. A. Meech, I. V. Samarasekera, J. K. Brimacombe, V. Rakocevic, *Ironmaking Steelmaking* **1999**, *26*, 269.
[176] G. Poltarak, S. Ferro, C. Cicutti, *Steel Res. Int*. **2017**, *88*. https//doi.org/10.1002/srin.201600223
[177] M. Bellet, A. Heinrich, *ISIJ Int*. **2004**, *44*, 1686.
[178] N. Triolet, M. Bobadilla, M. Bellet, L. Avedian, P. Mabelly, *Rev. Metall*. **2005**, *102*, 343.
[179] S. Koric, B. G. Thomas, V. R. Voller, *Numer. Heat Transfer B-Fundam*. **2010**, *57*, 396.
[180] J. D. Lee, C. H. Yim, *ISIJ Int*. **2000**, *40*, 765.
[181] K. Toishi, Y. Miki, *ISIJ Int*. **2016**, *56*, 1764.
[182] K. Liu, Q. S. Sun, J. Q. Zhang, C. Wang, *Metall. Res. Technol*. **2016**, *113*. https//doi.org/10.1051/metal/2016012
[183] K. Liu, C. Wang, G. L. Liu, N. Ding, Q. S. Sun, Z. H. Tian, *High Temp. Mater. Proc.-Isr.* **2017**, *36*, 359.
[184] A. Yamanaka, K. Nakajima, K. Okamura, *Ironmaking Steelmaking* **1995**, *22*, 508.
[185] Y. M. Won, T. J. Yeo, D. J. Seol, K. H. Oh, *Metall. Mater. Trans. B* **2000**, *31*, 779.
[186] M. Bellet, O. Cerri, M. Bobadilla, Y. Chastel, *Metall. Mater. Trans. A* **2009**, *40A*, 2705.
[187] T. Koshikawa, M. Bellet, C. A. Gandin, H. Yamamura, M. Bobadilla, *Metall. Mater. Trans. A* **2016**, *47A*, 4053.
[188] M. Bellet, G. H. Qiu, J. M. Carpreau, *J. Mater. Process. Technol*. **2016**, *230*, 143.
[189] B. G. Thomas, M. Bellet, in *ASM Handbook*, ASM International, Materials Park, OH **2008**, p. 449.
[190] Y. M. Won, B. G. Thomas, *Metall. Mater. Trans. A* **2001**, *32*, 1755.
[191] D. L. You, C. Bernhard, G. Wieser, S. Michelic, *Steel Res. Int*. **2016**, *87*, 840.
[192] C. Beckermann, *Int. Mater. Rev*. **2002**, *47*, 243.
[193] F. Mayer, M. Wu, A. Ludwig, *Steel Res. Int*. **2010**, *81*, 660.
[194] M. H. Wu, J. Domitner, A. Ludwig, *Metall. Mater. Trans. A* **2012**, *43A*, 945.
[195] J. Domitner, M. H. Wu, A. Kharicha, A. Ludwig, B. Kaufmann, J. Reiter, T. Schaden, *Metall. Mater. Trans. A* **2014**, *45A*, 1415.
[196] S. Luo, M. Y. Zhu, S. Louhenkilpi, *ISIJ Int*. **2012**, *52*, 823.
[197] Y. Zhao, R. S. Qin, D. F. Chen, X. M. Wan, Y. Li, M. T. Ma, *Steel Res. Int*. **2015**, *86*, 1490.
[198] D. J. Seol, K. H. Oh, J. W. Cho, J. E. Lee, U. S. Yoon, *Acta Mater*. **2002**, *50*, 2259.
[199] B. Bottger, M. Apel, B. Santillana, D. G. Eskin, *Metall. Mater. Trans. A* **2013**, *44A*, 3765.
[200] M. Yoshiya, M. Watanabe, K. Nakajima, N. Ueshima, K. Hashimoto, T. Nagira, H. Yasuda, *Mater. Trans*. **2015**, *56*, 1467.